

FULL PAPER

Open Access



Surface creep rate distribution along the Philippine fault, Leyte Island, and possible repeating of $M_w \sim 6.5$ earthquakes on an isolated locked patch

Yo Fukushima^{1*} , Manabu Hashimoto², Masatoshi Miyazawa², Naoki Uchida³ and Taka'aki Taira⁴

Abstract

Active faults commonly repeat cycles of sudden rupture and subsequent silence of hundreds to tens of thousands of years, but some parts of mature faults exhibit continuous creep accompanied by many small earthquakes. Discovery and detailed examination of creeping faults on land have been in a rapid progress with the advent of space-borne synthetic aperture radar interferometry. In this study, we measured the spatial variation of the creep rate along the Philippine fault on Leyte Island using ALOS/PALSAR data acquired between October 2006 and January 2011. Prominent creep of 33 ± 11 mm/year was estimated in northern and central parts of the island except for a locked portion around latitude $11.08\text{--}11.20^\circ$ N. We compared the creep rate distribution along the fault with the slip distribution of the 2017 M_w 6.5 Ormoc earthquake which occurred in northern Leyte, estimated from the displacements mapped by ALOS-2/PALSAR-2 interferometric data. The estimated slip of the 2017 earthquake amounted up to 2.5 m and to moment magnitude of 6.49, with the dominant rupture area coinciding with the locked portion identified from the interseismic coupling analysis. Teleseismic waveforms of the 2017 earthquake and another event that occurred in 1947 (M_s 6.9) exhibit close resemblance, indicating two ruptures of rather similar locations and magnitudes with a time interval of 70 years.

Keywords: Philippine fault, Leyte Island, Crustal deformation, SAR interferometry, InSAR, Fault creep, Repeating earthquake, Characteristic earthquake, Historical seismograms

Introduction

It has been known that faults accommodate a spectrum of fault slip from fast rupture of regular earthquakes to stable sliding, and slow earthquakes in between (e.g., Peng and Gomberg 2010; Avouac 2015). Earthquakes occurring on isolated patches within stably sliding area (repeating earthquakes or repeaters) have been widely found in various tectonic settings (e.g., Uchida and Bürgmann 2019). These repeaters are thought to occur on a velocity-weakening frictional patch surrounded by velocity-strengthening regions (Chen and Lapusta 2009).

Although large repeaters of $M \geq 6$ are more difficult to find than smaller ones because of smaller number of samples (Uchida and Bürgmann 2019), large repeaters would be valuable for studying earthquake physics because the rupture characteristics can be known in detail compared to smaller ones, for example by examining the micro-earthquakes that occur around large earthquake ruptures (Uchida et al. 2012). The periodicity of large repeaters may be of particular interest in the context of earthquake forecast, considering that some repeaters can be large enough to cause damages. Forecast of repeaters can be made more precisely than ordinary earthquakes because repeaters commonly occur on isolated asperities so that the repeat time is well explained by the creep rate of the surroundings (Nadeau and Johnson 1998; Uchida and Bürgmann 2019).

*Correspondence: fukushima@irides.tohoku.ac.jp

¹ International Research Institute of Disaster Science, Tohoku University, Aramaki Aza-Aoba 468-1, Aoba-ku, Sendai 980-8572, Japan
Full list of author information is available at the end of the article

The sequence of Parkfield $M \sim 6$ earthquakes in California, USA, which occurs in a transition zone between the creeping and locked segments along the San Andreas fault, is probably the most famous example of relatively large repeaters. In spite of quasi-regular occurrence until 1966, the earthquake prediction experiment, such that the “next one” would occur before 1993, failed with eventual occurrence in eleven years after the prediction window closure (Bakun et al. 2005). Nevertheless, the Parkfield earthquakes provide valuable insights into the physics of earthquake occurrence. Bakun et al. (2005) stated that the sequence of Parkfield earthquakes belong to the first class of characteristic earthquakes, having the same faulting mechanism, magnitude and occur on the same fault segment, but not to the second class of characteristic earthquakes that requires same hypocenter and rupture direction. As summarized by Harris (2017), other examples of relatively large earthquakes that occurred on faults with spatial variations in the degree of fault locking include 1868 M_w 6.8 Hayward earthquake (Bakun 1999), a few earthquakes in 1970s–1980s along Eureka Peak, Imperial, San Andreas, and Superstition Hills faults in Southern California (Louie et al. 1985), and multiple $M_w > 6.8$ events along the Longitudinal Valley Fault in Taiwan (Thomas et al. 2014a). Whether these earthquakes can be categorized as repeaters or not remains unclear.

In this paper, we claim that the 2017 M_w 6.5 Ormoc earthquake, that ruptured the Philippine fault in the northern part of Leyte Island and caused damages, was close to a first-class characteristic earthquake that ruptured an isolated locked segment within creeping sections. For that purpose, we first show results of Synthetic Aperture Radar (SAR) interferometry (InSAR) time-series analysis, which gives indication of fault creep along most part of the Philippine fault in northern Leyte. InSAR time-series analysis or stacking analysis using multiple SAR images has been successfully used to detect fault creeps including the San Andreas fault zone (e.g., Bürgmann et al. 1998; Lindsey et al. 2014a), Ismetpasa area of the North Anatolian fault (Çakir et al. 2005; Kaneko et al. 2013), Izmit section of the North Anatolian fault (Aslan et al. 2019; Cakir et al. 2012; Hussain et al. 2016), Chaman fault (Fattahi and Amelung 2016), El Pilar fault in Venezuela (Pousse Beltran et al. 2016), Haiyuan fault in China (Jolivet et al. 2012), and Longitudinal Valley fault in Taiwan (Hsu and Bürgmann 2006). Next, we show that the slip of the 2017 Ormoc earthquake occurred on the only locked portion of the fault in northern Leyte, by performing a fault slip model inversion and comparing the result with the creep distribution. Third, we show that the teleseismic waveforms of the 2017 earthquake and another earthquake in 1947, whose epicenter is located

about 20 km away, are remarkably similar, allowing us to hypothesize that characteristic earthquakes occur on this locked portion of the fault. Lastly, we make inference on the future seismic potentials of the Philippine fault on northern Leyte.

Tectonic settings and the two earthquakes in 1947 and 2017 along the Philippine fault on Leyte

The Philippine fault is a major left-lateral strike-slip fault that runs through the Philippine archipelago (Fig. 1). On the northwestern part, the Sunda Plate subducts along the Manila Trench west of the archipelago, whereas from the east the Philippine Sea Plate subducts underneath the archipelago along the Philippine Trench. The region bounded by the western and eastern trenches, sandwiched between the Philippine Sea and Sunda Plates, is referred to as Philippine Mobile Belt (Gervasio 1967), whose kinematics have been modeled with multiple blocks (Rangin et al. 1999; Galgana et al. 2007). The left-lateral component resulting from the oblique convergence of the Philippine Sea Plate and the archipelago is mainly accommodated by displacements along the Philippine Fault (Allen 1962; Barrier et al. 1991; Aurelio 2000).

It has been inferred that several large earthquakes have occurred along the Philippine fault (Acharya 1980). Some earthquakes along the fault were associated with surface ruptures and were studied in detail: 1973 M_s 7.4 Ragay Gulf earthquake (Tsutsumi et al. 2015), 1990 M_w 7.7 Luzon earthquake (e.g. Nakata et al. 1990; Shibutani 1991; Silcock and Beavan 2001), and 2003 M_s 6.2 Masbate earthquake (PHIVOLCS 2003) (Fig. 1). For example, the 1990 Luzon earthquake ruptured a segment of 125 km and caused severe damage including more than 2000 fatalities and numerous building collapses (Murrayama and Hirano 1993; CRED and Sapir 2001).

Along the Leyte section of the fault, some GPS studies have inferred creep (Duquesnoy et al. 1994; Catane et al. 2000; Bacolcol 2003). Besana and Ando (2005) also suggested the existence of fault creep by claiming that earthquakes of magnitudes larger than 6.0 had not occurred between the beginning of the seventeenth century and the moment of their writing. It must be noted, however, that the authors referred to a historical earthquake catalog published by the Southeast Asia Association of Seismology and Earthquake Engineering (SEASEE 1985), which had a data gap between 1942 and 1948. One of the focusing earthquakes in the present study, an M_s 6.9 event in 1947 in northern Leyte, was overlooked in the catalog and hence by Besana and Ando (2005). This event is included in the catalogs of ISC-GEM (Di Giacomo et al. 2018) and of the Philippine Institute of Volcanology and Seismology (PHIVOLCS 2018).

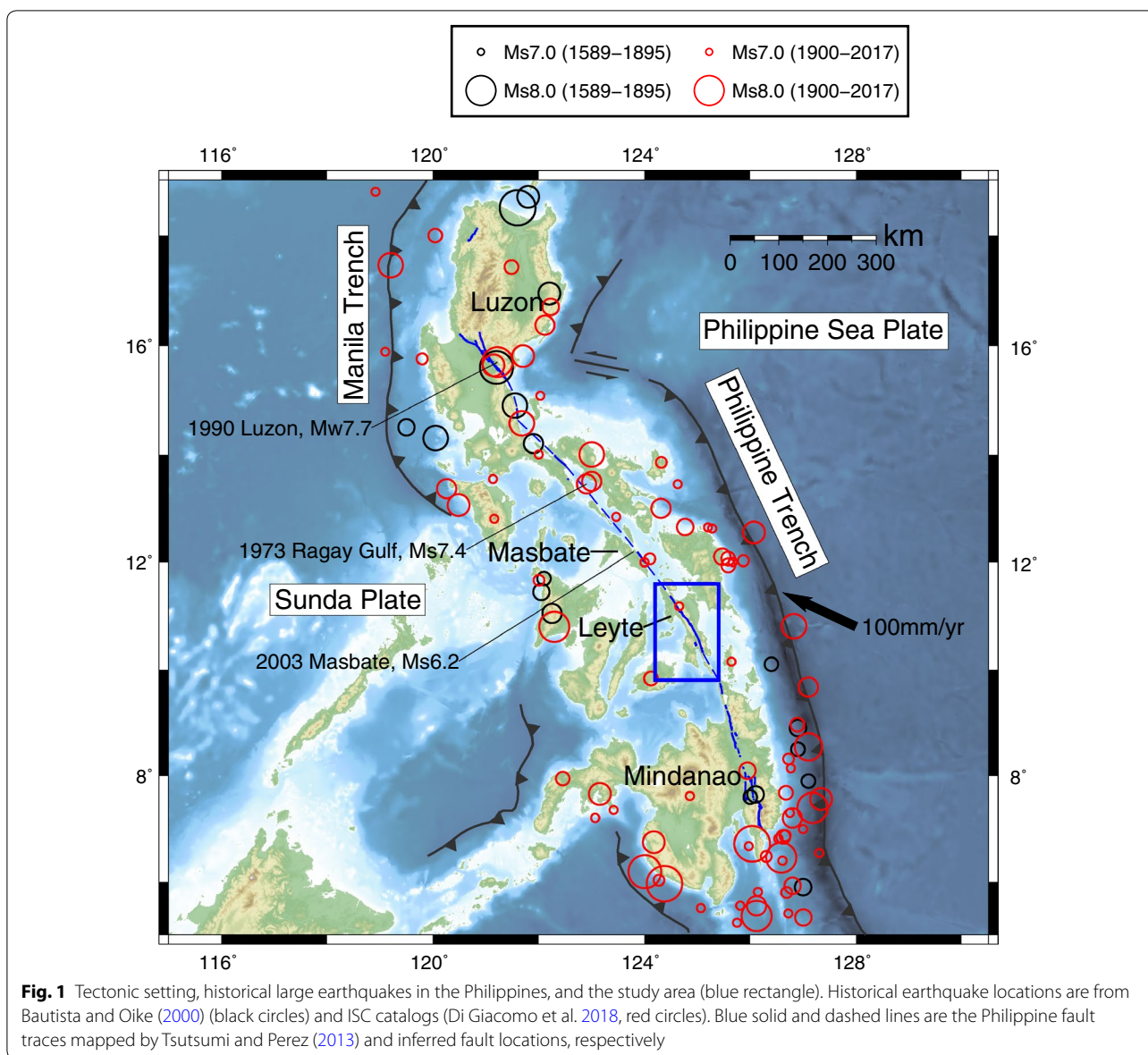


Fig. 1 Tectonic setting, historical large earthquakes in the Philippines, and the study area (blue rectangle). Historical earthquake locations are from Bautista and Oike (2000) (black circles) and ISC catalogs (Di Giacomo et al. 2018, red circles). Blue solid and dashed lines are the Philippine fault traces mapped by Tsutsumi and Perez (2013) and inferred fault locations, respectively

On 6 July 2017, an M_w 6.5 (M_s 6.5) earthquake struck the northern area of Leyte (Fig. 2, Table 1), close to the town of Ormoc (Yang et al. 2018). One of the nodal planes of its focal mechanism determined by the U.S. Geological Survey (USGS) is consistent with a rupture of the Philippine fault, with mainly NW striking left-lateral slip. Yang et al. (2018) obtained coseismic displacements of the 2017 earthquake from InSAR analyses of ALOS-2 and Sentinel-1A satellite data. They used the displacements measured by InSAR to infer the fault geometry and coseismic slip distribution of the earthquake. They estimated that the fault dip was 78.5° and the maximum slip was 2.3 m. According to their model, the main slip area was located at shallow depths

of less than 5 km, but their result also indicated slip at a deeper depth range of 4–16 km north of the main slip area.

The location of the 2017 earthquake is close to that of a M_s 6.9 earthquake that occurred on 7 June 1947 (Fig. 2, Table 1). To our best knowledge, the 1947 earthquake has not been studied in detail besides a seismological study of Lumbang and Hurukawa (2014), who relocated the event to be along the Philippine fault.

There are moderate topographic variations over the island, with a peak of 1403 m (Fig. 3). No strong contrast with respect to the location of the Philippine fault exists in the topography.

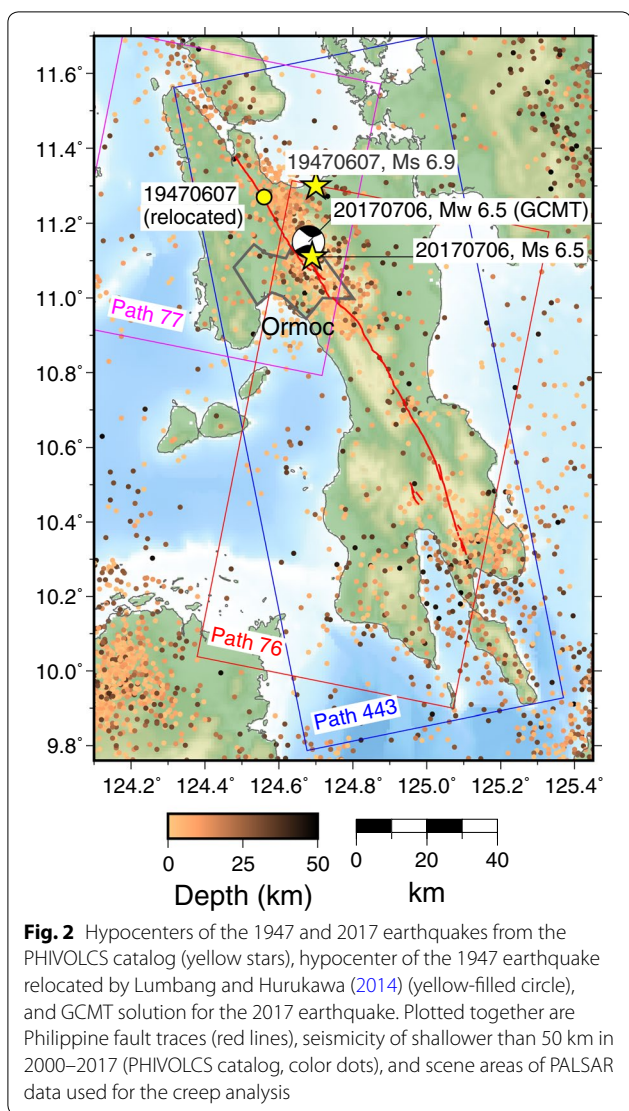


Fig. 2 Hypocenters of the 1947 and 2017 earthquakes from the PHIVOLCS catalog (yellow stars), hypocenter of the 1947 earthquake relocated by Lumbang and Hurukawa (2014) (yellow-filled circle), and GCMT solution for the 2017 earthquake. Plotted together are Philippine fault traces (red lines), seismicity of shallower than 50 km in 2000–2017 (PHIVOLCS catalog, color dots), and scene areas of PALSAR data used for the creep analysis

Analysis of interseismic coupling and surface creep

For the purpose of measuring the coupling and creep rate along the Philippine fault on Leyte Island, we used ALOS/PALSAR SAR data obtained between October 2006 and January 2011 from paths 443 (ascending), 76

(descending), and 77 (descending) (Fig. 4). We used 20, 5, 3 images for paths 443, 76, 77, respectively. The incidence angles of the acquisitions were all 38.8°.

We also tested using ALOS-2/PALSAR-2 data to capture the creep signal, but the longest-available temporal baseline of the pairs before the occurrence of the 2017 earthquake was 14 months because of the change in the radar wavelength in June 2015 (Natsuaki et al. 2016), which was too short to capture a clear signal. We did not attempt to use data of C-band satellites such as Envisat or Sentinel-1A because of the heavy vegetation on the island that causes decorrelation of the signals.

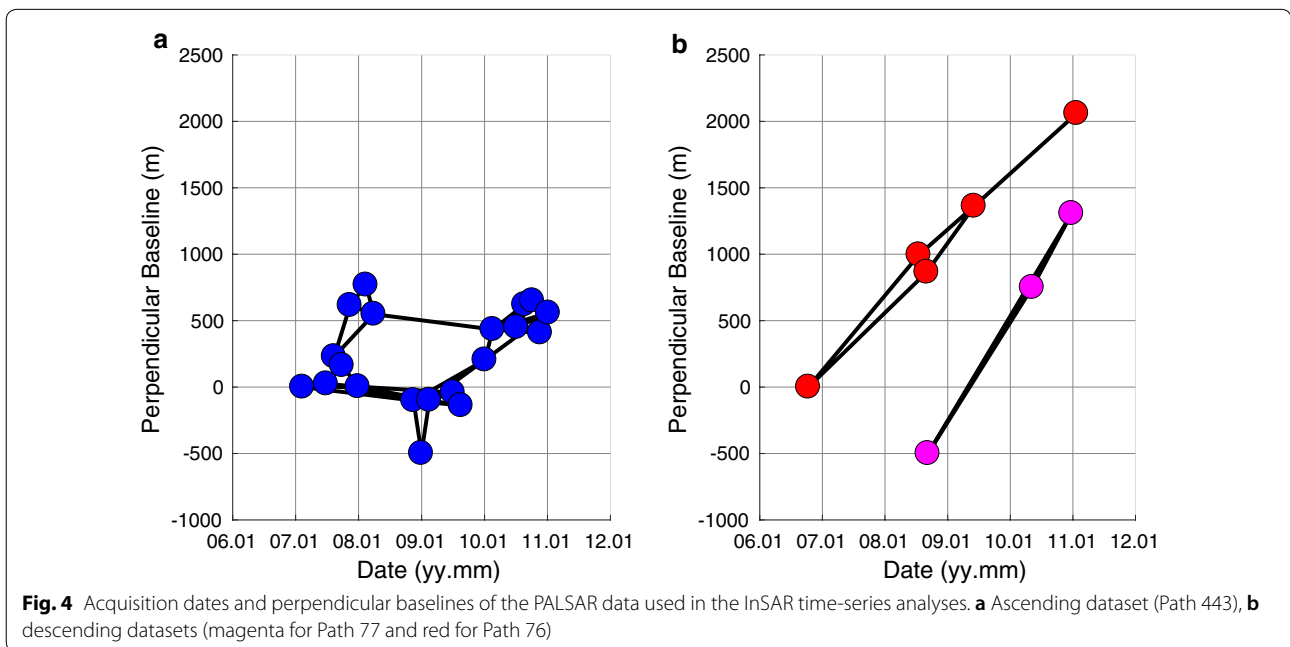
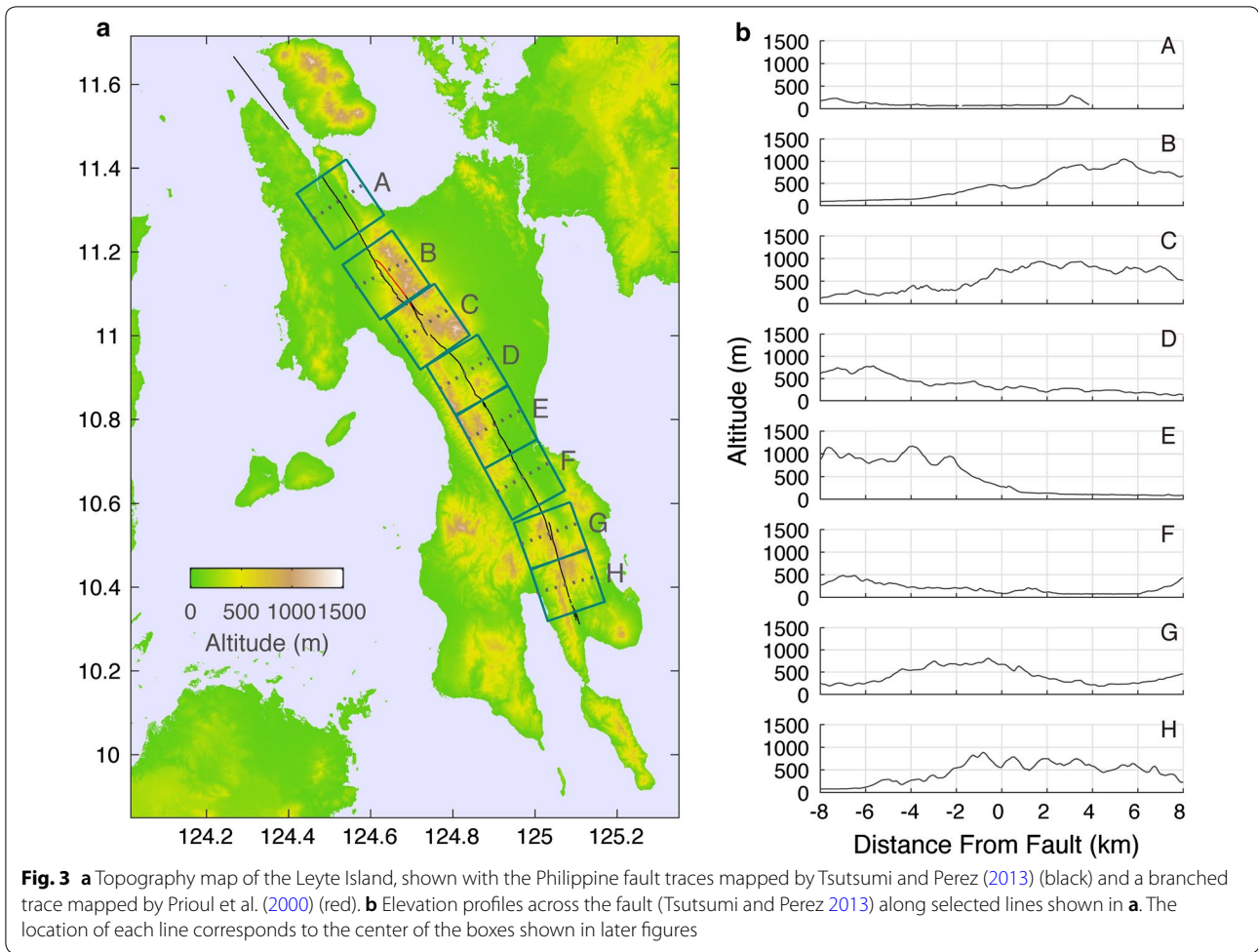
We used Gamma® software (Wegmüller and Werner 1997) for producing interferograms from ALOS SAR data. We used the digital elevation model SRTM version 4 (Jarvis et al. 2008) to remove the topographic fringes and to geocode the interferograms. To enhance the coherence of the signals, the geocoded interferograms were decimated (reduced size by taking the average of multiple pixels) in such a way that the final interferograms have pixel intervals of 15 arc seconds (approximately 450 m) in both longitude and latitude directions, and further low-pass filtered by taking a moving average of 3 × 3 pixels. As a result, the spatial resolution is approximately 1.5 km. Finally, phase unwrapping was applied using SNAPHU (Chen and Zebker 2000) to obtain the line-of-sight (LOS) displacements.

After creating small-baseline unwrapped interferograms, InSAR time-series analyses were conducted (See Appendix for the method) to derive the mean velocity field on almost the entire island of Leyte. We simultaneously solved for the unknown offsets and planar trends that originate from orbital inaccuracies and ionospheric perturbations in the interferograms to separate them from the displacement time-series. Examples of the detrended velocity maps as well as their mean velocity map are shown in Additional file 1: Figure S1. The velocity at each pixel was calculated by the linear least squares fitting to the displacement time-series. The results from two descending data sets were merged after obtaining the mean velocity (Additional file 1: Figure S2).

Table 1 Parameters of the 1947 and 2017 earthquakes

Earthquake	Source	Lat. (° N)	Lon. (° E)	Depth (km)	M _w	M _s
7 June 1947	PHIVOLCS	11.3	124.7	33	–	6.9
	ISC-GEM	11.1824	124.6575	15.0	–	7.0
	LH ^a	11.27 ± 0.12	124.56 ± 0.14	15.0	–	–
6 July 2017	PHIVOLCS	11.11	124.69	2	–	6.5
	USGS	11.127 ± 6.9 km	124.629 ± 6.9 km	9.0 ± 1.8 km	6.5	–
	Global CMT	11.15	124.68	12.0	6.5	6.5

^a Lumbang and Hurukawa (2014)

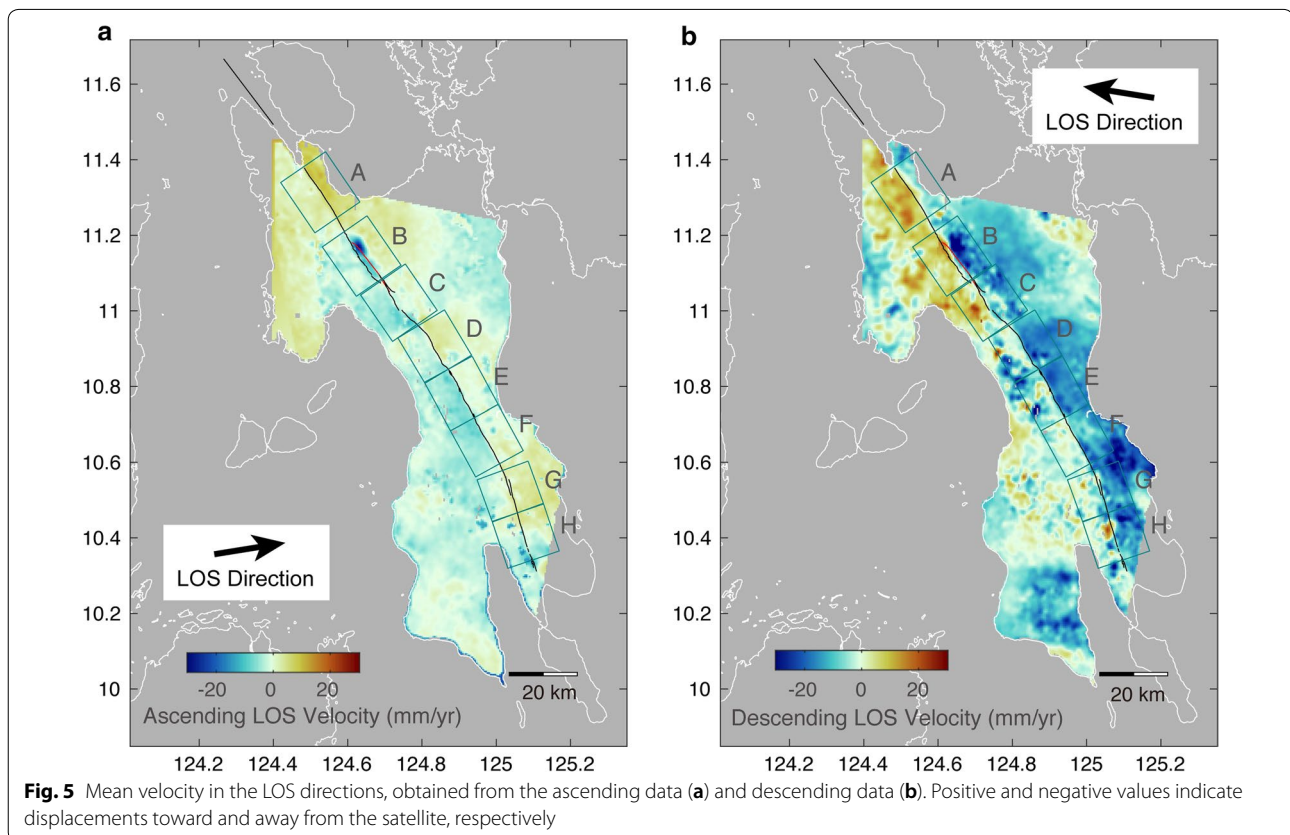


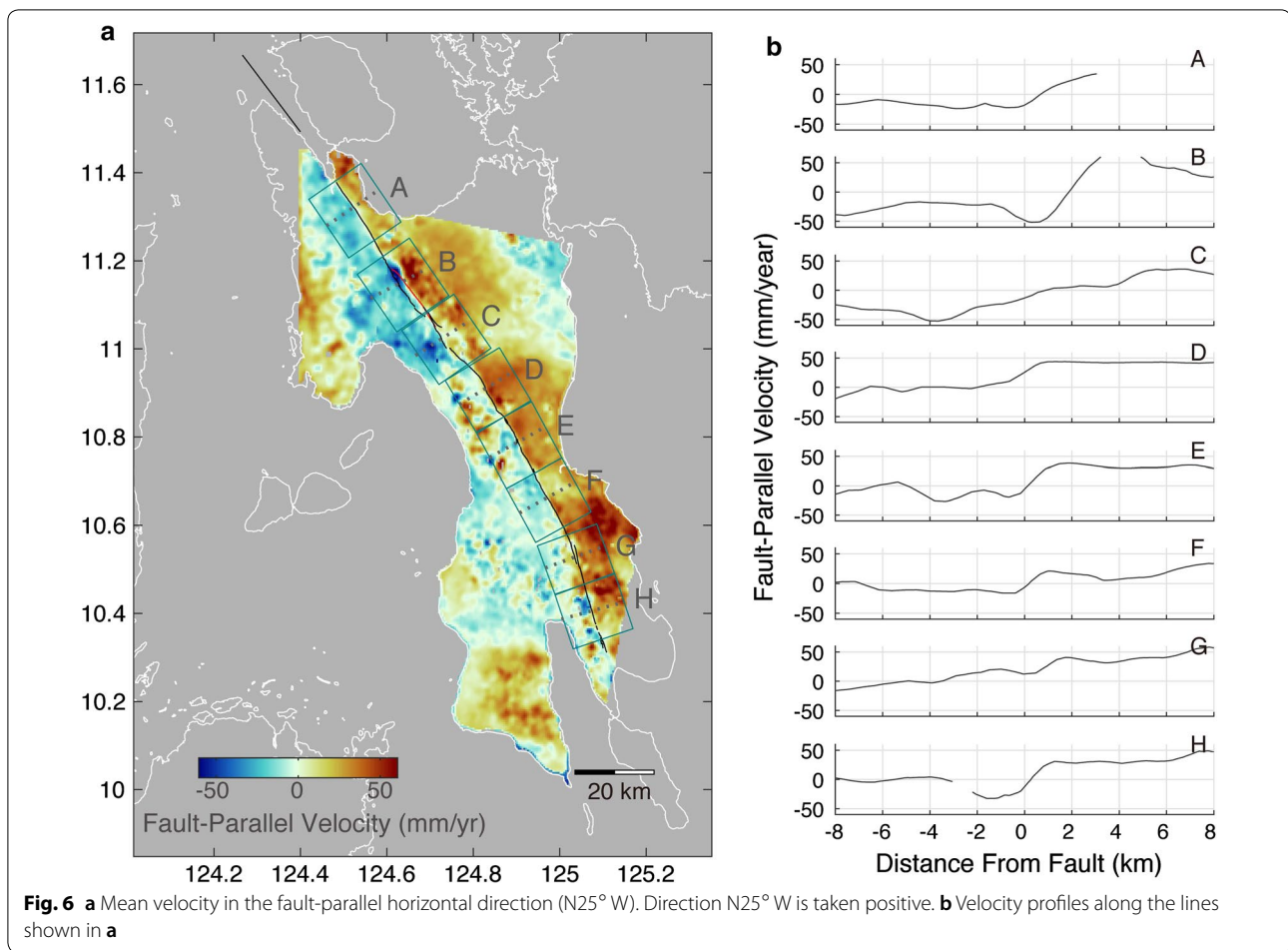
The mean velocity fields estimated using the data from the two LOS directions show clear velocity offsets across the fault (Fig. 5). In spite of the fact that the creep signal seen from the ascending orbit is faint (this is due to the nearly perpendicular sense of motion with respect to the LOS direction), we can recognize the velocity contrast across the fault in the ascending result thanks to suppressed noise originating from the large number of used data (Fig. 5a). The geometrical relation between the LOS direction and the creep movement is much more favorable for the descending orbit data, and the creep signal is recognized even though the noise level is large due to a small number of data (Fig. 5b). The velocity uncertainties estimated for the ascending and descending datasets were ~ 2 mm/year for most of the areas, and spatially variable in a range of 2–10 mm/year, respectively (Additional file 1: Figure S3).

From the average velocity maps from the ascending and descending directions, we decomposed the velocity field into east–west and quasi-vertical components (Fujiwara et al. 2000). For a visualization purpose, the east–west velocity was further converted to fault-parallel horizontal velocity by assuming that the ground only displaces in the fault-parallel direction, which was assumed to be N25° W. While this assumption is

reasonable for most of the analyzed area, it may not be the case for some parts adjacent to the fault where the velocity field is complex. Figures 6 and 7 shows the velocity fields in fault-parallel horizontal and quasi-vertical components, hence, obtained. Here, the quasi-vertical direction is 8.9° inclined to the south from the pure vertical direction. The fault-parallel horizontal velocity field clearly shows discontinuity across the Philippine fault, whereas the quasi-vertical field does not (Figs. 6, 7). The lack of offsets in the quasi-vertical component indicates that the velocity estimates in the ascending and descending directions were not systematically biased by the tropospheric delay or other effects.

In the fault-parallel horizontal velocity field (Fig. 6a), velocity contrast across the fault is clearly recognized except for the sections around latitude 11.0° N (Boxes B–C) and at the southern tip (Box H). In the profiles (Fig. 6b), velocity transition widths of 1–2 km across the fault are observed instead of sharp offsets. We consider that this is mainly due to the spatial averaging described earlier, but we cannot exclude the possibility that the fault does not have a sharp structure up to the surface and the deformation is distributed across a finite shear zone (Lindsey et al. 2014b).



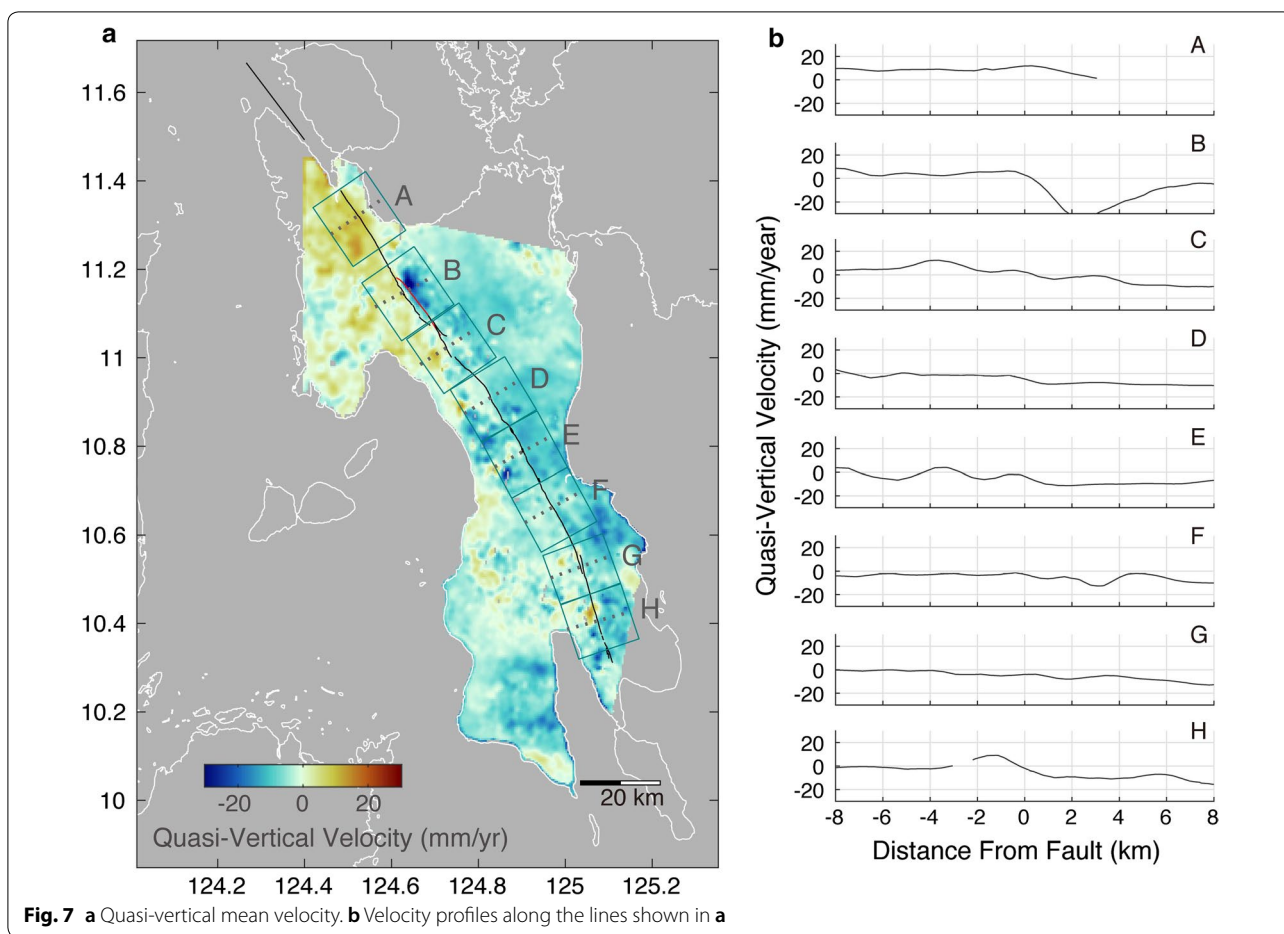


We measured the surface creep rate along the fault in the following manner, using the ascending and descending velocity maps (Fig. 5a, b) independently. First, we defined rectangular cells of 2 km in length (perpendicular to fault) and 1 km in width (parallel to fault) on each side of the fault, along the entire fault (Fig. 8). Here, we adopted a smooth curve that approximates the fault traces mapped by Tsutsumi and Perez (2013) which had some step-overs. The distance between the rectangles and the fault was set to be 0.5 km. Since the length of the Philippine fault on Leyte is approximately 138 km, 138 pairs of cells were defined along the fault. Next, we obtained the velocity offsets by taking the difference of the average velocity values in the pairing cells facing each other across the fault. The location of the cells as well as the velocity profiles are shown in Fig. 8. Finally, the velocity offsets were converted to the fault creep rate by assuming left-lateral motion.

The results from the two directions show consistent creep rates (Fig. 9). Rates of 20–50 mm/year were obtained at the northern-most area (Box A) and in the central area (Box D–F). The mean creep rates obtained

along these sections in the ascending, descending and both data sets were 32 ± 10 mm/year, 34 ± 12 mm/year, and 33 ± 11 mm/year, respectively.

We could not estimate the creep rate at latitudes of 11.13–11.18° N (in Box B) with the method because of a subsidence signal of ~ 35 mm/year due to probable operations of geothermal power plants on the area to the east of the fault. This section appears to be a fault relay zone, having a western branch mapped by Tsutsumi and Perez (2013) and an eastern branch proposed by Prioul et al. (2000), offset by approximately 200 m. A closer look into the fault-parallel horizontal velocity field (Fig. 10) indicates no velocity contrast across the western branch of the fault, suggesting that this branch is locked during the interseismic period. A velocity contrast is rather visible along the eastern branch, suggesting creep continuing from the south, although a part of this signal is probably associated with the local subsidence. Interestingly, claystone, which is a compelling candidate for explaining the mechanism of fault creep (Thomas et al. 2014a; Avouac 2015; Kaduri et al. 2017), has been found on the western side of this creeping section at depths greater than



1 km (Prioul et al. 2000). As will be shown later, the 2017 earthquake ruptured the locked western branch between a latitude range of 11.08–11.20° N.

In the southern-most part of the island (southern half of Box G and Box H), the uncertainty in the creep estimation is large, and the creep, if any, was above our detection limit. The large uncertainty is because of the fault strike being nearly perpendicular to the ascending LOS direction resulting in insensitivity to the fault motion from the ascending direction (Fig. 5a), and because of large apparent atmospheric noise in the mean velocity obtained from the descending data (Figs. 5b, 8).

The creep rate of 33 ± 11 mm/year obtained in northern and central Leyte compares well with results of previous studies using GNSS (26 ± 10 mm/year (Duquesnoy et al. (1994), 1991–1993), 36 ± 0.2 mm/year [Bacolcol (2003), 1991–2002]), and alignment arrays (21–27 mm/year, Tsutsumi et al. (2016), 2013–2016). Considering that the average displacement rate in northern Leyte is about 20 mm/year over the last half a million years (Aurelio 1992) and that a block modeling analysis estimated 21 mm/year of relative motion of blocks separated by the

Philippine fault (Aurelio 2000), our results together with previous geodetic estimates indicate “full” creep, i.e., no slip deficit accumulation, on the detected creeping sections.

Analysis of the 2017 Ormoc earthquake slip

For the purpose of estimating the fault slip distribution of the 6 July 2017 earthquake, we used the ascending and descending ALOS-2/PALSAR-2 images, both obtained with right-looking mode, used in a previous study (Yang et al. 2018). Our main emphasis was put on comparing the extent and amount of the fault slip of the 2017 earthquake with what we obtained in the coupling and creep analysis described in the previous section. Yang et al. (2018) used Sentinel-1A data in addition to the ALOS-2/PALSAR-2 data. We did not use the Sentinel-1A data in our analysis because of its low coherence and apparent long-wavelength atmospheric noise.

Table 2 shows the parameters of the used data. The second images of the interferograms were acquired nine days after the earthquake, indicating that they may be slightly

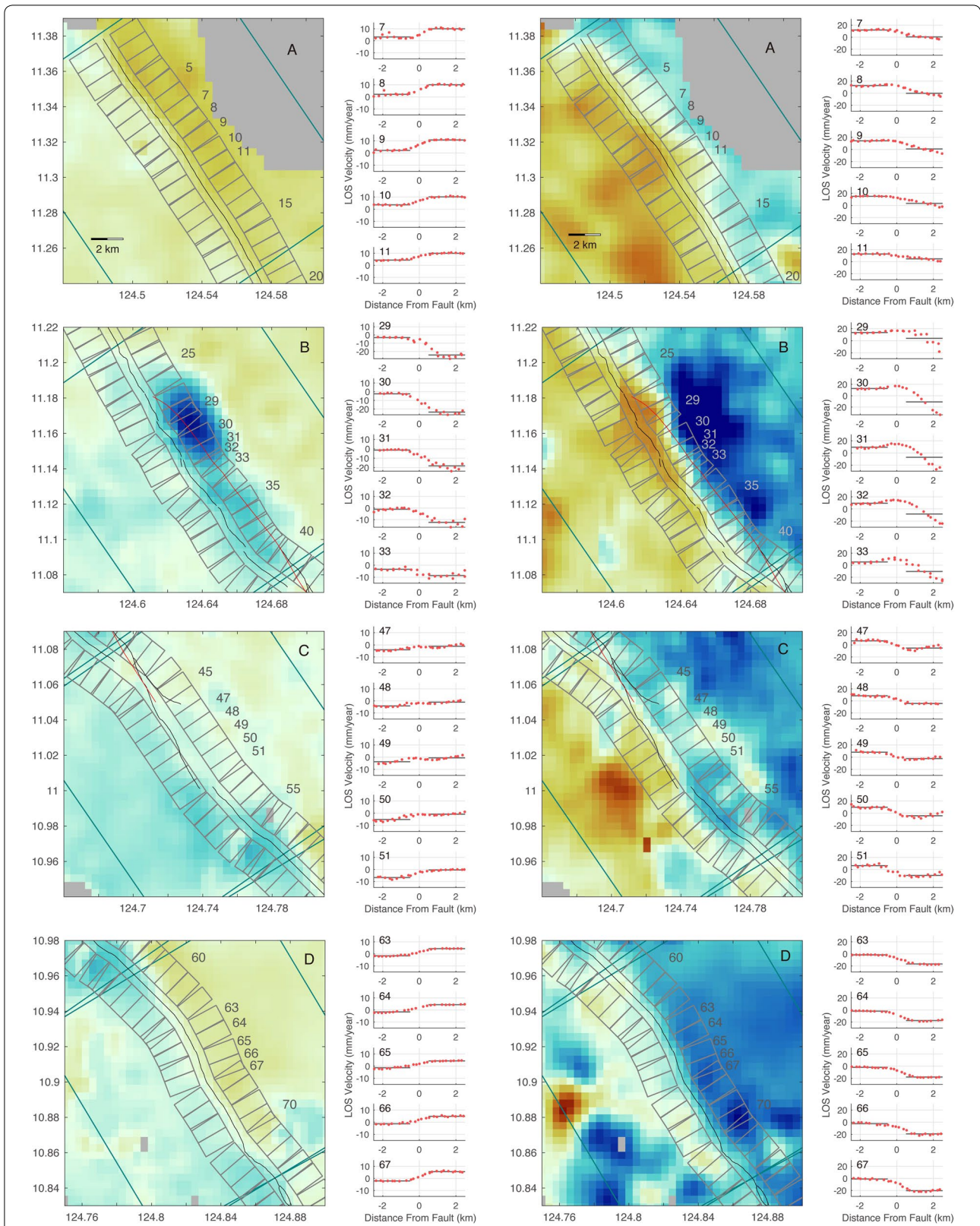


Fig. 8 Zoom-up figures of the ascending and descending mean velocity maps with the location of the rectangular cells used for the profile analysis, and selected velocity profiles. The location of the cells were numbered starting from north (1) to south (138). In the velocity profile figures, the velocity values within the cells are plotted, as well as the average velocity on each side of the fault denoted in black lines

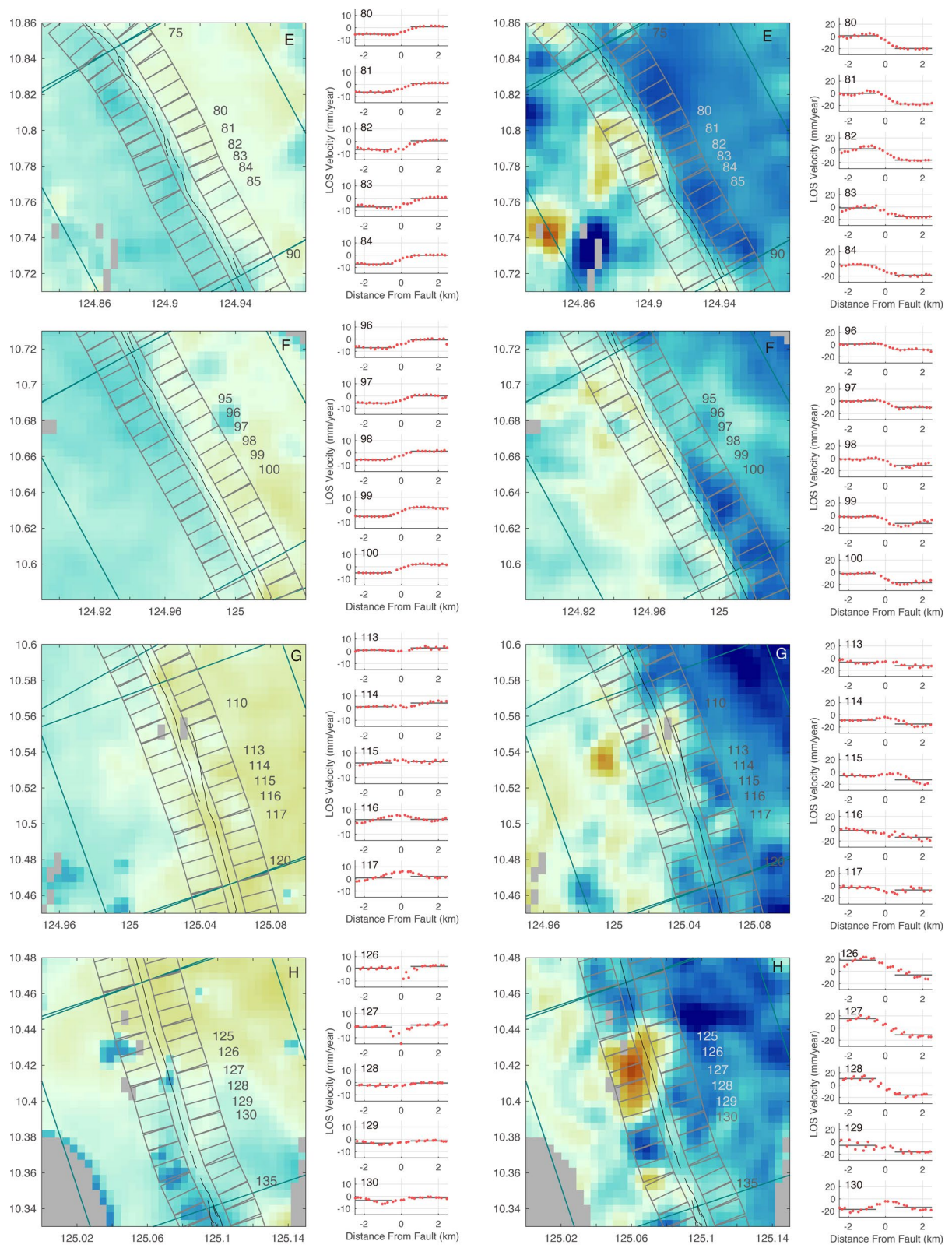
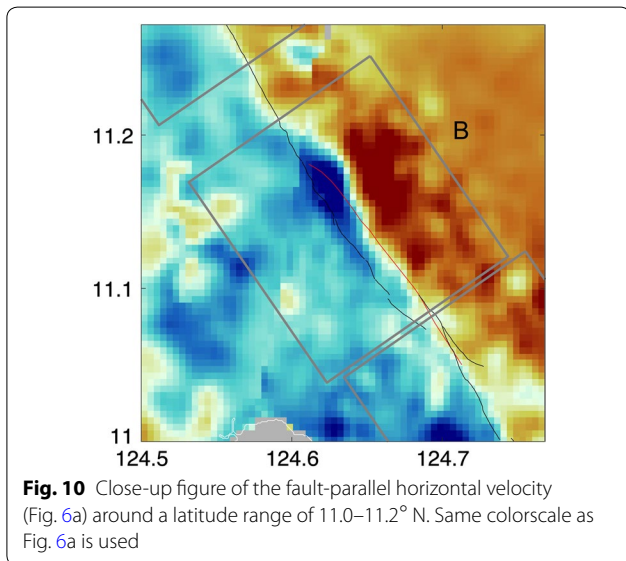
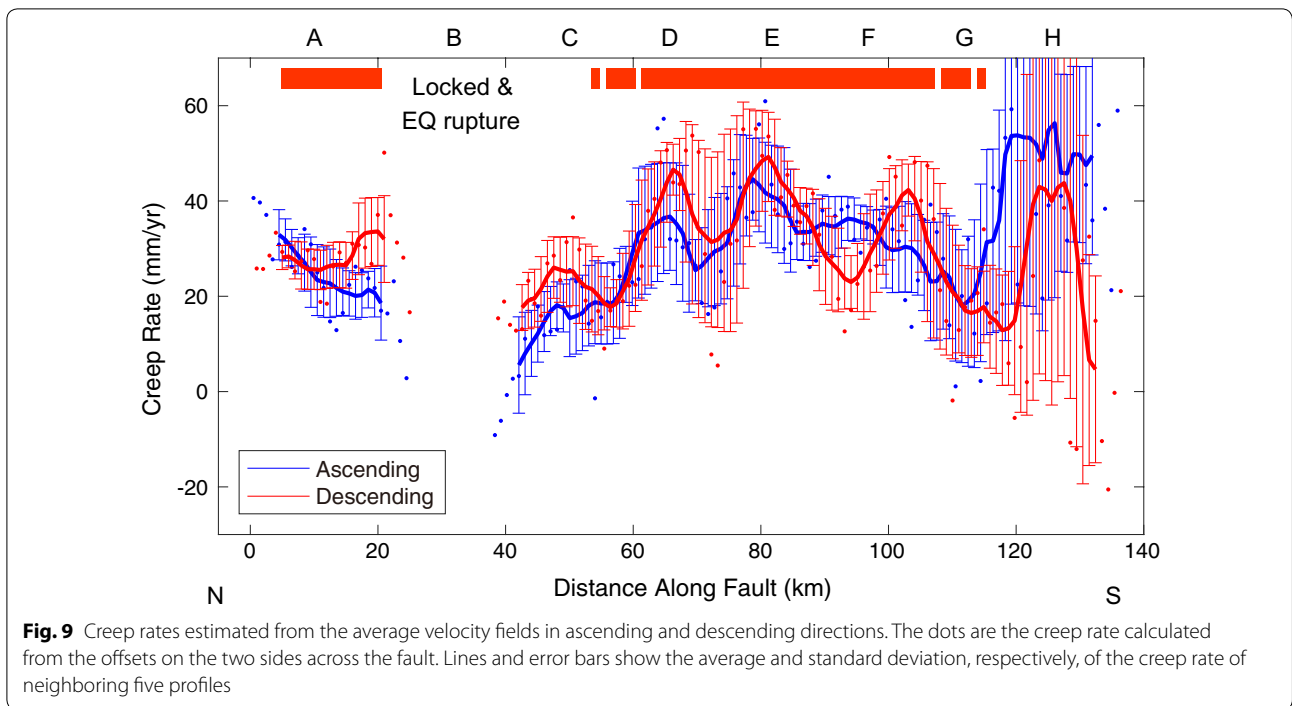


Fig. 8 continued



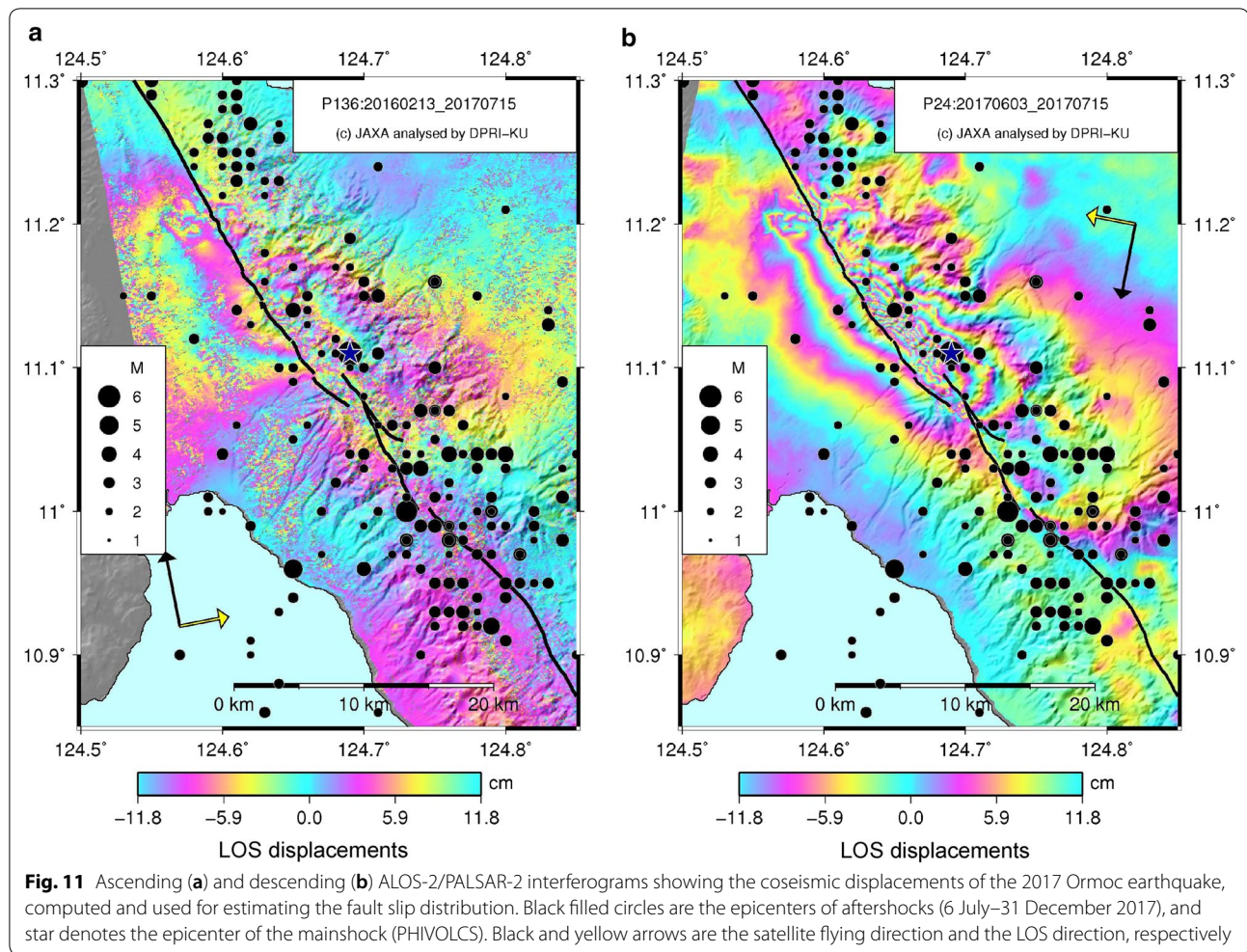
contaminated by post-seismic displacements. In this study, we assumed that post-seismic displacements are negligible compared to coseismic ones.

We conducted a 2-pass interferometry with Gamma[®] software (Wegmüller and Werner 1997). We multi-looked ascending images by 9 and 12 in the range and azimuth directions, respectively, and descending images by 9 and 10, to enhance coherence at the cost of reduction in spatial resolution. Digital Ellipsoidal Height Model developed by T. Tobita (Geospatial Information Authority of Japan) and T. Ozawa (National Research Institute for Earth Science and Disaster Resilience of Japan) based on Digital Elevation Model of SRTM 4.1 was used for geocoding and computation of topographic phase. We flattened interferograms by applying polynomial functions, and unwrapped them with the branch-cut algorithm using Gamma's[®] modules. Correlation threshold of 0.8 was adopted to reduce unwrapping error. Finally, quad-tree subsampling was applied to prepare data for inversion (see Additional file 1: Figures S4, S5).

Figure 11 shows the ascending and descending interferograms. We recognize asymmetric pattern of fringes across the surface trace of the Philippine fault. The comparison with the mapped fault traces clearly indicates rupture of the western branch of the fault relay

Table 2 ALOS-2/PALSAR-2 data used for computing the interferograms of the 2017 earthquake

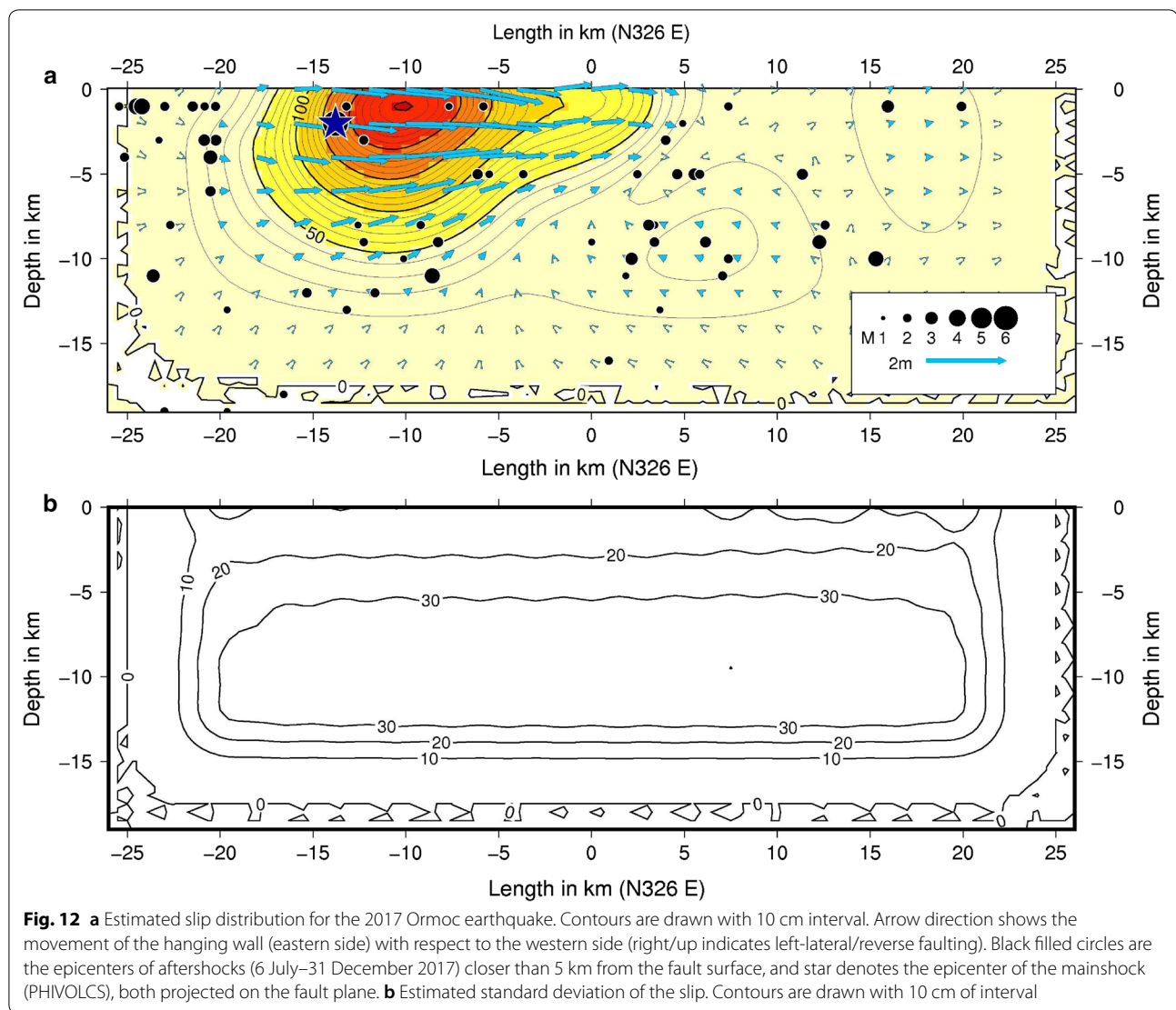
Orbit direction	Path	Frame	Incidence angle (°)	Dates (yy.mm.dd)	Perpendicular baseline (m)
Ascending	136	210–220	31.4	16.02.13–17.07.15	32.3
Descending	24	3390–3400	36.3	17.06.03–17.07.15	9.0



zone at a latitude range of 11.08–11.20° N (see Additional file 1: Figure S6 for a close-up comparison with the fault traces), which coincides with the extent of Box B defined in the creep analysis described earlier. The ascending interferogram shows decrease of LOS displacements on the eastern side and increase on the western side, whereas the descending interferogram shows increase of LOS displacements on the eastern side and decrease on the western side. This pattern of deformation is consistent with left-lateral strike-slip motion of the Philippine fault. However, there are many complexities of fringes in the vicinity of the epicenter, which implies complex geometry of the surface rupture. Because of the low coherence, we could not unwrap the phase properly in the complex fault-vicinity area. In the following, we will not discuss deformation in this fault-vicinity area. The density of aftershocks is relatively higher around the northern and southern ends of the deformed zone (Fig. 11).

We inverted the interferograms with the method of Fukahata and Wright (2008). This method assumes a single fault plane and estimates its dip angle, smoothing hyperparameter, and slip distribution simultaneously based on Akaike Bayesian Information Criterion (ABIC), with the strike angle and location of the fault fixed. In our case, the strike angle of the fault could be fixed to that of the Philippine fault, because the discontinuities of observed fringes well corresponded to the fault. We set the top side of the model fault with a length of 50 km along the surface trace of the Philippine fault. The depth range of the model fault was set to 0–20 km. We did not use data in the area within 3 km from the surface trace of the Philippine fault, where unwrapping errors could be suspected.

We searched for the optimal solution which minimizes ABIC in the range of dip angle from 40° to 90° with a step of 2°. Figure 12 shows the estimated slip distribution of the optimal model on a vertical cross section along the strike of N34° W. The optimal dip angle was estimated as 74°, dipping to the east. We



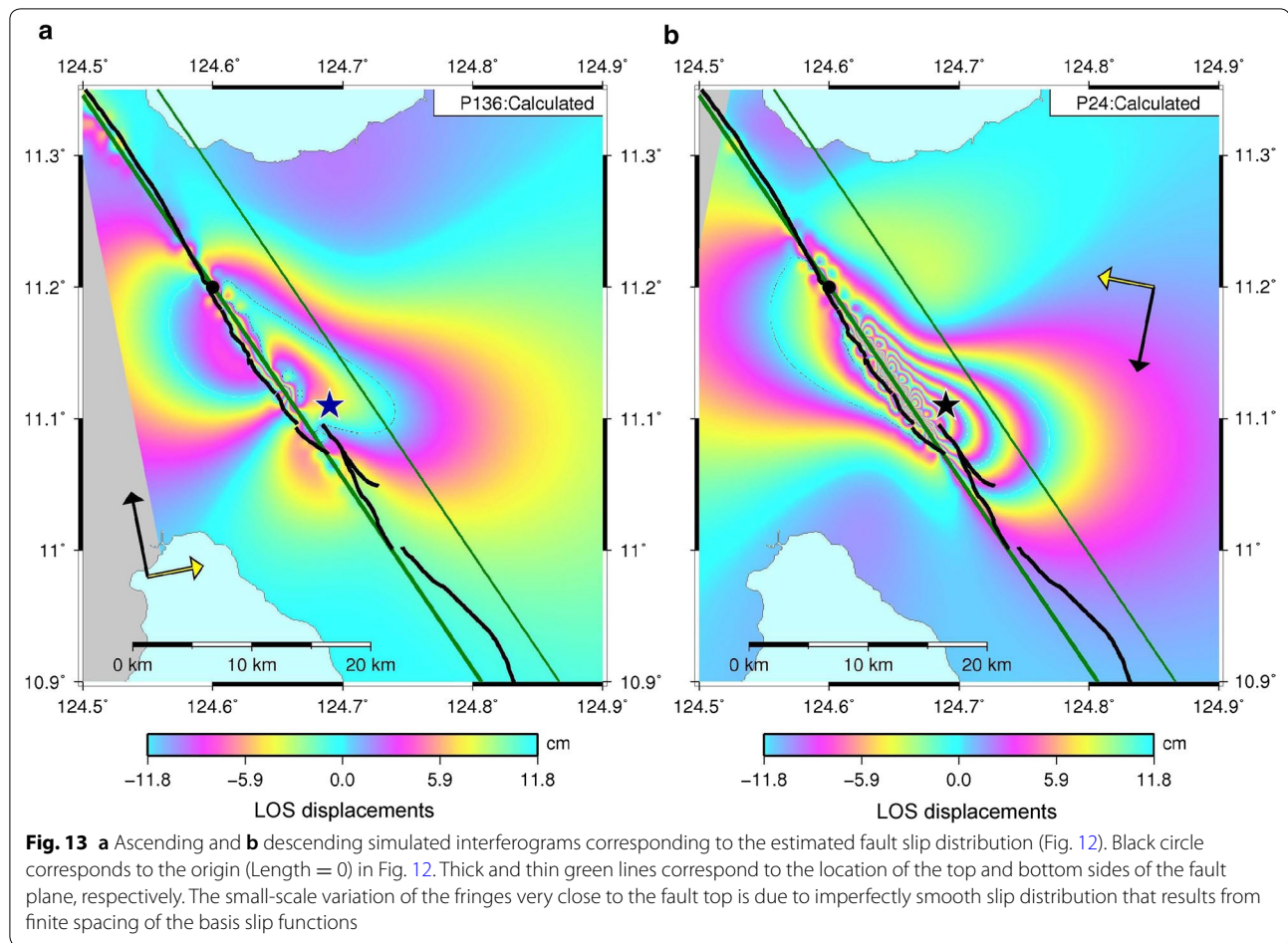
obtained up to ~ 2.5 m of almost purely left-lateral strike slip. The horizontal extent of the rupture at the surface is approximately 25 km, and the depth extent is limited to less than 10 km. These features are similar to the slip distribution estimated by Yang et al. (2018), except that the model of Yang et al. (2018) has another slip patch with average slip of 0.4 m at depths of 4–16 km. Slip on the same area is suppressed in our model. We speculate that the deeper slip in the model of Yang et al. (2018) is an artifact enhanced by long-wavelength noise in the Sentinel-1A data. In our model, the slip in the deeper patch is smaller than the model uncertainty (Fig. 12b). The geodetic moment was estimated to be $6.80 \pm 1.46 \times 10^{18}$ Nm (M_w 6.49).

This model well reproduces the InSAR observation, except for the nearest areas from the surface trace of the Philippine fault (Fig. 13). The horizontal extent

of the area with coseismic slip above 0.5 m well corresponds to the western fault in Box B which appears locked during the interseismic period (Fig. 10). We can, therefore, interpret that the earthquake occurred as a result of stress concentration caused by the fault creep at both northern and southern sides of the 2017 rupture segment as in Parkfield (Barbot et al. 2012). The aftershocks are located mainly in the surroundings of the large slip area (Fig. 12a).

Comparison of the waveforms of the 1947 and 2017 earthquakes

The 2017 earthquake was located 21–23 km away from the epicenter of the 1947 event (Fig. 2, Table 1). It has been known that the epicenters in global earthquake catalogs can be mislocated by as much as a few tens of kilometers (Biggs et al. 2006). For this reason, we do not



exclude the possibility that the true epicenters of the 1947 and 2017 earthquakes are much closer to each other. In this section, we compare the teleseismic waveforms of 1947 and 2017 earthquakes observed at Abuyama (western Japan), Oshu (northeastern Japan), and Berkeley (western United States).

At Abuyama observatory of Kyoto University (34.84° N, 135.57° E), a Wiechert seismograph was in operation and recorded waveforms continuously between 1932 and 1991 (Yamazaki 2001). Figure 14a shows the vertical waveform of the 1947 event. Clear onset of P wave and large amplitudes of the Rayleigh wave are visible. The waveforms of the 2017 event were recorded with a Streckeisen STS-2 broad-band seismograph of F-net, operated by the National Research Institute for Earth Science and Disaster Resilience, Japan (National Research Institute for Earth Science and Disaster Resilience 2019), deployed at a location 100–200 m from the site of the 1947 recording. We applied a convolution filter on the waveform to simulate the response of Wiechert seismograph (see Table 3 for the response parameters), which is compared to that of the 1947

event (Fig. 14a). Though the time scale of the 1947 event waveform was not recorded, we estimated it by linearly stretching or compressing the time axis of the 2017 event so that the 2017 event waveform matches the 1947 event waveform. The waveforms are similar to each other including later phases.

The waveforms of P and Rayleigh waves are proportionally similar between two events. We measured the amplitudes of P and Rayleigh waves recorded on the vertical component. The peak-to-peak amplitude ratios of Rayleigh wave to P wave for the 1947 and 2017 events are 1.8 (7 mm/4 mm) and 1.84 (4.6 mm/2.5 mm), respectively. These consistencies indicate that the fault mechanism and depth of the earthquakes are similar for the two events. The Rayleigh wave amplitude of the 1947 event is approximately 1.5 times larger, in other words the ratio of seismic moments is 1.5, indicating that the moment magnitude of the 1947 event is about 6.7. This is a conservative estimate because we were not able to correct for the friction of the pendulum, which would lead to larger magnitude of the 1947 event if applicable. Judging from waveforms and difference in magnitudes, two events are

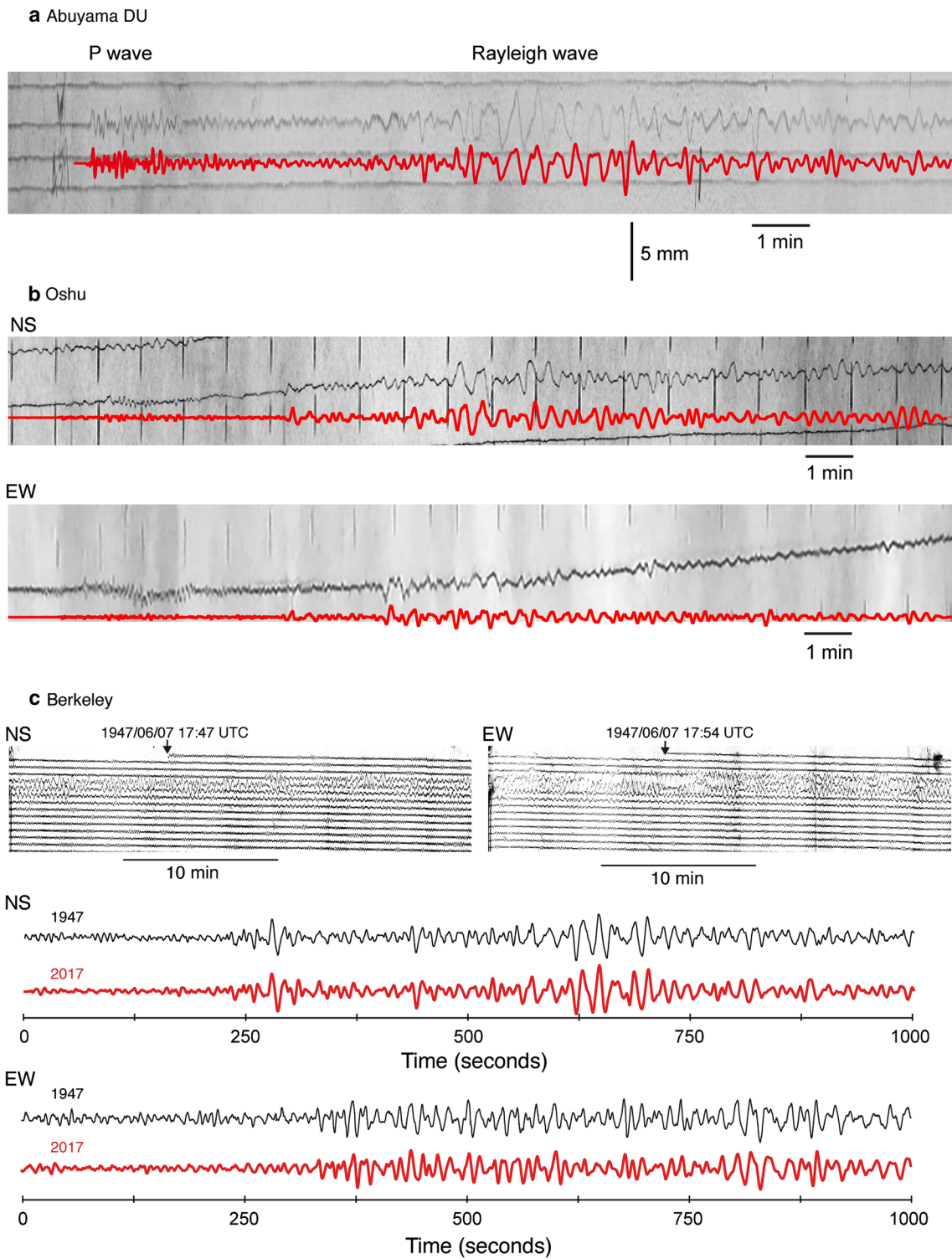


Fig. 14 Comparisons of the seismograms of the 1947 and 2017 events recorded at three sites in Japan and USA. For each comparison, black and red show seismograms of the 1947 and 2017 events, respectively. **a** Abuyama, western Japan, vertical (down-up) component. **b** Oshu, northeastern Japan, horizontal components. **c** Berkeley, California, USA, horizontal components

close in location and with similar mechanism, but not perfectly identical in the rupture area.

At Oshu, an Omori-type seismograph operated in the Mizusawa Astronomical Observatory (39.13° N, 141.13° E) recorded the horizontal waveforms of the 1947 event (Fig. 14b). No vertical seismograph was in operation at the site then. The 1947 waveforms were compared with the ones observed by an STS-2 seismograph operated at Esashi station of Tohoku University (39.15° N, 141.33° E), 18 km east of the Mizusawa observatory. We applied a convolution filter on the STS-2 waveforms to simulate the response of Omori seismograph (Fig. 14b, see Table 3 for response parameters). Since the damping parameter was unknown, we tested with different values and adopted the one that produces the waveforms similar to the 1947 waveforms. As shown in the figure, similar waveforms were obtained especially for the NS component.

Two Leyte earthquakes were also recorded in the Western Hemisphere. At a station in Berkeley, California, USA (37.87° N, 122.26° W), Wilip–Galitzin and STS-2 seismometers well registered event signals in horizontal components from the 1947 and 2017 earthquakes, respectively. The Wilip–Galitzin instrument response mainly consisted of seismometer and galvanometer (McComb and Wenner 1936). For the Wilip–Galitzin horizontal seismometers, the corner periods for both seismometer and galvanometer were calibrated to be 12 s (Bolt and Miller 1975). The damping coefficients of them were set to be the near critical damping (1.0) (Uhrhammer, personal communication). The STS-2 sensor has a corner period of ~120 s and a damping coefficient of ~0.70 for all three components, and has a flat amplitude response up to ~10 Hz (Berkeley Digital Seismic Network 2014). Unlike Abuyama and Oshu recordings, Berkeley paper records required to be digitized to improve the resolution of waveforms. We used DigitSeis software developed by Bogiatzis and Ishii (2016) to convert scanned paper records into digital time-series data. For the 2017 STS-2 records, the instrument response was deconvolved to obtain ground velocity, and then the Wilip–Galitzin instrument response was convolved to generate synthesized 2017 Wilip–Galitzin records. The synthesized records are very similar to the 1947 Wilip–Galitzin

records in the two horizontal components (Fig. 14c). It should be noted that the amplitude levels from the 1947 earthquake at the station were not constrained well. Bolt and Miller (1975) documents that the magnification value for the Berkeley Wilip–Galitzin horizontal records is 1000 at the corner period of 12 s; however, the uncertainty of the magnification would range from 5 to 10% (Uhrhammer, personal communication).

In conclusion, the teleseismic waveforms of the 1947 and 2017 earthquakes recorded at three different sites, after correction for the instrumental response, showed close similarity, from which we suggest overlap in the fault rupture areas of the two earthquakes.

Discussion

Mechanism of locking and creeping of the Philippine fault on the northern and central parts of Leyte Island

As summarized by Avouac (2015) and Harris (2017), the occurrence of fault creep has been explained using a range of physical and chemical processes. Hydrothermal flow, causing reduction of effective normal stress on the fault, has been proposed as a possible mechanism of fault creep on Leyte (Duquesnoy et al. 1994), just as other sites such as southern California (Donnellan et al. 2014) or Asal Rift (Gjibouti) (Dobre and Peltzer 2007). A high geothermal gradient near the eastern branch in Box B (red curve in Fig. 10) and much less geothermal gradient to the west (Prioul et al. 2000) is also consistent with this hypothesis. As described earlier, presence of claystone (Prioul et al. 2000) is another compelling candidate for the mechanism of the creep. Lithological investigations along the creeping and locked portions such as done by Thomas et al. (2014b) and Kaduri et al. (2017) would be of interest for constraining the creep mechanism of the Philippine fault.

Recently, numerical simulation studies assuming rate-and-state friction laws have shown that parallel faults, as is the case for the Box B section, interact with each other to produce both fast and slow-slip events (Romanet et al. 2018; Mitsui 2018). A result of the simulation studies indicates that the locking of the ruptured patch in Box B may have resulted from the geometrical effect. Capturing the deformation of this area in the future will enable us to

Table 3 Specifications of the seismographs for the 1947 Leyte earthquake

Site	Angular distance from the epicenter	Azimuth (epicenter to station)	Seismometer	Period (s)	Damping factor
Abuyama	25.5°	N21° E	Wiechert DU	4.7	0.45
Oshu	31.4°	N25° E	Omori NS	36	2.0 ^a
(Mizusawa)			Omori EW	16	2.0 ^a
Berkeley	100.5°	N48° E	Wilip–Galitzin	12	1.0

^a Estimated by trials and errors

evaluate the contribution of the geometrical effect on the fault slip behaviors.

Seismic potential in northern and central Leyte

In the previous sections, we showed that (1) the Philippine fault in northern and central Leyte has been creeping with a rate of 33 ± 11 mm/year, with the exception of a locked segment within a major 15-km-long step-over section (Box B, latitude 11.08° N– 11.20° N, Fig. 10), (2) the 2017 earthquake occurred along the Philippine fault and the rupture extent well corresponds to the locked section (Fig. 12), and (3) the 1947 earthquake ruptured a similar area on the fault. The two earthquakes of 1947 and 2017 do not exactly fall in the definition of the “first class characteristic earthquakes” (Bakun et al. 2005) which requires the same magnitude for the repeating earthquakes and waveforms’ similarity, but the small difference in the magnitudes (M_s 6.9 and 6.7 determined by PHIVOLCS (2018)) is consistent with a nearly characteristic nature.

We cannot completely exclude the possibility that an earthquake rupture may propagate a sizable distance into creeping zones as was suggested by Noda and Lapusta (2013), but no prominent evidence of such cases has been found so far (see the summaries by Avouac (2015) and Harris (2017)). Assuming, here, that fully creeping sections cannot host earthquakes, the maximum possible extent of rupture would be the ~ 30 -km-long locked and partially creeping section between latitudes of 11.08° N and 11.20° N. The stepover (~ 200 m) of the fault at a latitude of 11.1° N is small enough to be easily jumped over (Shaw and Dieterich 2007).

Harris (2017) showed that the scaling law of strike-slip faults proposed by Wells and Coppersmith (1994)

$$M_w = 5.16 + 1.12 \log(L), \quad (1)$$

where L is the fault length, holds on earthquakes along creeping faults. This scaling law appears to be applicable for the 2017 Ormoc earthquake, as the magnitude derived from the scaling law (M_w 6.48, assuming the fault length of 15 km) is close to the value obtained from our fault slip model (M_w 6.49). If the rupture extends further to the south into Box C so that the fault length gets doubled, the predicted moment magnitude would be M_w 6.81. This value is consistent with our estimate of the moment magnitude for the 1947 event, $M_w \geq 6.7$, obtained from the waveform comparison. The 1947 earthquake (M_s 6.9), therefore, is inferred to be the maximum class in northern and central Leyte, rupturing the extent of Box B, C.

The 1947 and 2017 earthquakes are 70 years apart. With our estimated slip rate of 33 mm/year, the fault would accumulate 2.3 m of slip deficit in 70 years. This

value is similar to the amount of slip estimated for the 2017 rupture (maximum of 2.5 m), again consistent with the characteristics of repeating earthquakes.

Detection of creep using InSAR time-series analysis

The condition for detecting fault creep along the Philippine fault in Leyte with InSAR was not ideal, because (1) the study area is prone to decorrelation in the InSAR signal due to heavy vegetation, (2) the ascending LOS direction was close to perpendicular to the fault strike, leading to small sensitivity to the fault motion, (3) the number of descending images was small and we could not suppress noise mainly originating from the atmospheric disturbance.

The decorrelation problem was overcome by taking spatial averaging with a large window size. The resulting coarse resolution of ~ 1.5 km was still acceptable for the purpose of this study. The insensitivity problem in the ascending data set was overcome by suppressing the noise using a large number of images. The relatively larger noise in the result from the descending data set (resulting from small number of images) was compensated by the nearly ideal LOS direction being nearly parallel to the fault strike.

A key factor as to the detectability of signal in the presence of noise is the wavelengths of the signal and noise. Usually, the largest noise source in SAR interferograms is the atmospheric disturbance, which is spatially correlated. The fault creep signal, in contrast, has a sharp discontinuity being different from the noise characteristics, enabling extraction of signal out of noise. We did not attempt to estimate the fault creep distribution on the fault plane as has been done along the San Andreas fault zone (e.g., Ryder and Bürgmann 2008; Shirzaei and Bürgmann 2013), because the ground displacements caused by locking or creeping at depth have spatially smooth patterns that are often indistinguishable from the atmospheric noise. For Leyte, having much more abundant data especially from the descending orbit would enable to obtain the locking/creeping distribution on the fault at depth.

Conclusions

We measured the surface creep rate distribution along the Philippine fault on Leyte Island using InSAR time-series analysis. On the northern and central parts of the island, prominent creep of 33 ± 11 mm/year was estimated, roughly consistent with previous GNSS (Duquesnoy et al. 1994; Bacolcol 2003) and field measurements (Tsutsumi and Perez 2013). Comparison with the average tectonic loading rate on the fault in half a million years (Aurelio 1992) and with the block modeling

result (Aurelio 2000) indicates that the fault is fully creeping in northern-most and central parts of Leyte.

We also revealed that there was a locked portion in northern Leyte on the western branch of the fault relay zone, and that the 2017 M_w 6.5 earthquake ruptured this locked patch. We further found similarities in the hypocenter locations and waveforms of the 2017 event and an M_s 6.9 event in 1947, suggesting repeating ruptures within the same locked patch.

We inferred that the size of the 1947 earthquake (M_s 6.9) probably belongs to the maximum class in the northern and central Leyte. This study demonstrates the usefulness of fault creep/locking analysis using InSAR time-series analysis to evaluate the possible scenarios for the extent and magnitude of large earthquake occurrences. Both accumulation of archived satellite data and new SAR images acquired with more advanced radar equipment will lead to more reliable and detailed estimation of seismic potentials of creeping faults.

Supplementary information

Supplementary information accompanies this paper at <https://doi.org/10.1186/s40623-019-1096-5>.

Additional file 1. Additional figures.

Acknowledgements

We used the PALSAR and PALSAR-2 data shared among the PALSAR Interferometry Consortium to Study our Evolving Land Surface (PIXEL). The data were provided by the Japan Aerospace Exploration Agency (JAXA) under a cooperative research contract with the Earthquake Research Institute of the University of Tokyo. We used the F-net waveform data of the National Research Institute for Earth Science and Disaster Resilience. Berkeley seismic data for this study come from the Berkeley Digital Seismic Network (BDSN), doi: 10.7932/BDSN, operated by the UC Berkeley Seismological Laboratory, which is archived at the Northern California Earthquake Data Center (NCEDC), doi: 10.7932/NCEDC. We are grateful to H. Tsutsumi of Doshisha Univ. and J. Perez of PHIVOLCS for various helps including the active fault data, earthquake catalog, and discussion. We also thank International Latitude Observatory of Mizusawa and Yoshiaki Tamura for providing the historical seismic records of Mizusawa observatory, Tomotsugu Demachi for managing the record, R. Uhrhammer and J. Taggart of Univ. California, Berkeley for helping to identify historical seismic records at Berkeley. This study was partially supported by the Japan Society for the Promotion of Sciences KAKENHI Grant Number JP18K03795. We thank the two anonymous reviewers for constructive comments, which greatly helped to improve the quality of the paper.

Authors' contributions

YF conducted the fault creep analysis and led the preparation of the paper. MH conducted the analysis of the 2017 earthquake slip. MM, NU, and MT conducted the comparison of the waveforms of the 1947 and 2017 earthquakes, recorded at Abuyama, Oshu, and Berkeley, respectively. All authors read and approved the final manuscript.

Funding

This study was partially supported by the Japan Society for the Promotion of Sciences KAKENHI Grant Number JP18K03795.

Availability of data and materials

The datasets used and/or analyzed during the current study are available from the authors upon request.

Ethics approval and consent to participate

Not applicable.

Consent for publication

Not applicable.

Competing interests

The authors declare that they have no competing interests.

Author details

¹ International Research Institute of Disaster Science, Tohoku University, Aramaki Aza-Aoba 468-1, Aoba-ku, Sendai 980-8572, Japan. ² Disaster Prevention Research Institute, Kyoto University, Gokasho, Uji 611-0011, Japan. ³ Graduate School of Science, Tohoku University, Aramaki Aza-Aoba 6-6, Aoba-ku, Sendai 980-8578, Japan. ⁴ Berkeley Seismological Laboratory, University of California, Berkeley, 219 McCone Hall, Berkeley, California 94720-4760, USA.

Appendix

Appendix A. InSAR time-series analysis method

Fundamental observation equations

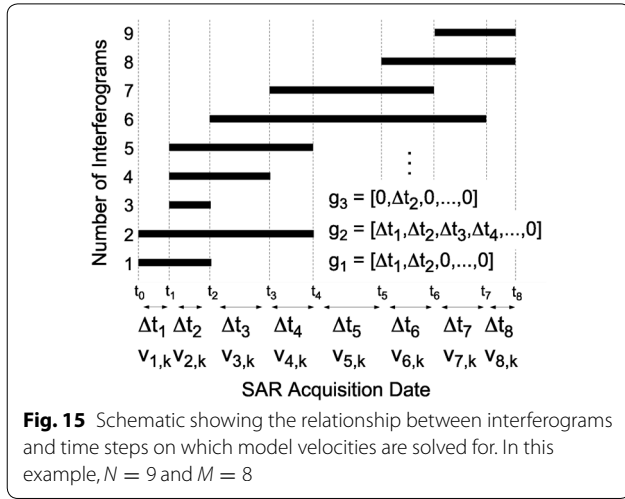
InSAR time-series analysis uses multiple interferograms produced from multiple pairs of SAR images. Each interferogram contains LOS ground displacements, an unknown offset, a phase ramp mainly due to orbital inaccuracy, atmospheric noise, and artifacts due to the errors of the digital elevation (or ellipsoidal height) model. We derive a formulation for jointly estimating the contributions from all of them, starting from unwrapped interferograms either in radar or geographic coordinates.

We approximate the phase ramp to be planar in the two dimensions (range and azimuth, or longitude and latitude). As for the atmospheric noise, we can consider the most prominent effect of the tropospheric stratification and can assume that the tropospheric phase delay is proportional to the altitude. The tropospheric and the height error terms should be introduced with care, as this can lead to spurious displacements if there are systematic variations in topography or topographic error. In our study, we did not estimate these terms, but the terms are considered in the following formulation for the sake of generality. The sum of the error components of the i th interferogram at k th pixel can be modeled as

$$d_{i,k}^{err} = a_i + b_i x_k + c_i y_k + f_i h_k + \delta h_k q_{i,k}, \quad (2)$$

where a_i , b_i , c_i , and f_i are constants for each i (constant over all the pixels), h_k is the altitude at the k th pixel (constant over all i), x_k is the distance in the x direction (e.g., range) from the origin of the interferogram (e.g., upper-left corner) to the k th pixel, y_k is the distance in the y direction (e.g., azimuth) measured from the origin, and $q_{i,k}$ is a factor that defines the sensitivity to the error of the digital elevation model

$$q_{i,k} = \frac{B_{\perp i,k}}{R_{i,k} \sin \theta_{i,k}}, \quad (3)$$



with $B_{\perp i,k}$, $R_{i,k}$ and $\theta_{i,k}$ denoting the perpendicular baseline, absolute range to ground points for the master acquisition, and incidence angle, respectively. The first term on the right-hand side of Eq. (2) correspond to the unknown offset, second and third terms to the planar phase ramp, fourth term to the delay due to tropospheric stratification, and the last term to the contribution of the digital elevation model error.

Then the observed LOS displacement of the i th interferogram at k th pixel can be written as

$$\begin{aligned} d_{i,k} &= \mathbf{g}_i \mathbf{v}_k + d_{i,k}^{err} + \epsilon_{i,k} \\ &= \mathbf{g}_i \mathbf{v}_k + \mathbf{s}_k \mathbf{r}_i + \delta h_k q_{i,k} + \epsilon_{i,k}, \end{aligned} \quad (4)$$

where $\mathbf{v}_k = [v_{1,k}, v_{2,k}, \dots, v_{M,k}]^T$ is the model velocity vector at k th pixel for M time steps defined by the SAR acquisition dates, \mathbf{g}_i is a vector that represents the time coverage of the i th interferogram; for example, when the i th interferogram spans the first two time windows, $\mathbf{g}_i = [\Delta t_1, \Delta t_2, 0 \dots 0]$, where $\Delta t_1, \Delta t_2, \dots$ represents the lengths of the time windows, $\epsilon_{i,k}$ is the unmodeled noise, and $\mathbf{s}_k = [1, x_k, y_k, h_k]$, $\mathbf{r}_i = [a_i, b_i, c_i, f_i]^T$.

See also Fig. 15 for explanation of our parametrization. Note that we can reduce the elements of \mathbf{s}_k and \mathbf{r}_i if we do not want to model certain nuisance terms, or can add more elements if, for example, we want to model the displacement ramp terms as quadratic functions.

We continue to put together the observation equations. Let P the number of pixels in each interferogram, N the number of interferograms, $\mathbf{d}_i = [d_{i,1}, d_{i,2}, \dots, d_{i,P}]^T$, data vector for all the pixels for i th interferogram, $\mathbf{v} = [\mathbf{v}_1^T, \mathbf{v}_2^T, \dots, \mathbf{v}_P^T]^T$, model displacement vector for all the time steps and all the pixels, $\delta \mathbf{h} = [\delta h_1, \delta h_2, \dots, \delta h_P]^T$, model vector of the DEM errors for all the pixels, $\epsilon_i = [\epsilon_{i,1}, \epsilon_{i,2}, \dots, \epsilon_{i,P}]$, noise vector.

Then, putting Eq. (4) together for all k leads to

$$\begin{aligned} \mathbf{d}_i &= \begin{bmatrix} \mathbf{g}_i & 0 \\ & \mathbf{g}_i \\ & \ddots \\ 0 & & \mathbf{g}_i \end{bmatrix} \begin{bmatrix} \mathbf{v}_1 \\ \mathbf{v}_2 \\ \vdots \\ \mathbf{v}_P \end{bmatrix} + \begin{bmatrix} \mathbf{s}_1 \\ \mathbf{s}_2 \\ \vdots \\ \mathbf{s}_P \end{bmatrix} \mathbf{r}_i \\ &+ \begin{bmatrix} q_{i,1} & & 0 \\ & q_{i,2} & \\ & & \ddots \\ 0 & & & q_{i,P} \end{bmatrix} \delta \mathbf{h} + \epsilon_i \quad (5) \\ &= \mathbf{G}_i \mathbf{v} + \mathbf{S} \mathbf{r}_i + \mathbf{Q}_i \delta \mathbf{h} + \epsilon_i. \end{aligned}$$

Finally, we put together the observation equations for all i ,

$$\begin{aligned} \mathbf{d} &\equiv \begin{bmatrix} \mathbf{d}_1 \\ \mathbf{d}_2 \\ \vdots \\ \mathbf{d}_N \end{bmatrix} = \begin{bmatrix} \mathbf{G}_1 & \mathbf{S} & & \mathbf{Q}_1 \\ \mathbf{G}_2 & & \mathbf{S} & \mathbf{Q}_2 \\ \vdots & & & \vdots \\ \mathbf{G}_N & & & \mathbf{S} \mathbf{Q}_N \end{bmatrix} \begin{bmatrix} \mathbf{v} \\ \mathbf{r}_1 \\ \mathbf{r}_2 \\ \vdots \\ \mathbf{r}_N \\ \delta \mathbf{h} \end{bmatrix} + \epsilon \\ &= \mathbf{G} \mathbf{m} + \epsilon. \end{aligned} \quad (6)$$

The model parameters in \mathbf{m} are solved with a linear inversion with the minimum norm constraint, as done by Berardino et al. (2002). The inverse problem is solved with singular value decomposition (SVD),

$$\hat{\mathbf{m}} = \mathbf{G}^+ \mathbf{d}, \quad (7)$$

where \mathbf{G}^+ is the pseudoinverse matrix of \mathbf{G} . The displacements can be obtained by simply multiplying elements of \mathbf{v} with the lengths of the time windows. Note that, when the interferograms are not separated into subsets, i.e., all the used SAR data are connected to each other with the network of interferometric pairs, the minimum norm constraint is unnecessary and the solution of Eq. (7) would be identical to a least-squares solution.

Denuisance from simultaneous inversion

The size of the matrix \mathbf{G} is $(NP) \times ((M+1)P + 4N)$, and solving the solution for all P pixels is not manageable in normal situations. We therefore adopted a two-step approach, first estimating the nuisance terms $\mathbf{r}_1, \mathbf{r}_2, \dots, \mathbf{r}_N$ with subsampled pixel points, and then estimating the LOS velocities \mathbf{v} and DEM errors $\delta \mathbf{h}$ for every pixel using the ‘‘corrected’’ displacements $\mathbf{d}^c = \mathbf{d} - \mathbf{d}_{sim}$, where the contributions from the nuisance terms \mathbf{d}_{sim} are subtracted from the original. The first step is to exactly follow Eqs. (2–6) with subsampled points. A regular-gridded subsampling, e.g., taking a pixel per every hundred pixels, would be appropriate.

Denuisance with GNSS time series

This step is an alternative to the method described above, and is not conducted in the present study. This method has been proposed by Fukushima and Hooper (2011) and used by Takada et al. (2018). The method is explained here for clarifying the relation with the alternative method.

If GNSS displacement data are available on the target area, the first step of the previous inversion method (denuisance) can be performed without jointly inverting for the LOS ground velocities. In general, this leads to more precise results if the spatial coverage of GNSS measurements is dense enough, because the joint inversion method has a risk of interpreting a part of the real deformation signals as the error terms if the signals have components of a planar trend or are correlated with altitude.

We assume that the GNSS time series have negligible errors compared to interferograms. Then, the GPS displacement in the SAR LOS direction that occurred in the same spanning period as the i th interferogram is $d_{i,k}^{GPS} = \mathbf{g}_i \mathbf{v}_k$, at a location corresponding to the k th pixel of the interferograms. From Eq. (4),

$$d_{i,k} - d_{i,k}^{GPS} = \mathbf{s}_k \mathbf{r}_i + \delta h_k q_{i,k} + \epsilon_{i,k}. \tag{8}$$

The observation equations (6) are simplified to be

$$\mathbf{d} - \mathbf{d}^{GPS} = \begin{bmatrix} \mathbf{S} & & \mathbf{Q}_1 \\ \mathbf{S} & & \mathbf{Q}_2 \\ & \ddots & \vdots \\ \mathbf{S} & \mathbf{Q}_N & \end{bmatrix} \begin{bmatrix} \mathbf{r}_1 \\ \mathbf{r}_2 \\ \vdots \\ \mathbf{r}_N \\ \delta \mathbf{h} \end{bmatrix} + \boldsymbol{\epsilon}, \tag{9}$$

where the InSAR data vector \mathbf{d} should now be subsampled at pixels that coincide with GPS station locations. Equation (9) is solved with the SVD method as in Eq. (7).

Estimation of ground displacements and DEM errors

After the denuisance, we only need to consider $\delta h_k q_{i,k}$ in Eq. (2) as the error source. In this case, the observation equations (6) can be separated into equations for each pixel. The relationship between the observed data and model parameters for the k th pixel is

$$\mathbf{d}_k^c \equiv \begin{bmatrix} d_{1,k}^c \\ d_{2,k}^c \\ \vdots \\ d_{N,k}^c \end{bmatrix} = \begin{bmatrix} \mathbf{g}_1 & q_{1,k} \\ \mathbf{g}_2 & q_{2,k} \\ \vdots & \vdots \\ \mathbf{g}_N & q_{N,k} \end{bmatrix} \begin{bmatrix} \mathbf{v}_k \\ \delta h_k \end{bmatrix} + \boldsymbol{\epsilon}_k \tag{10}$$

$$= \mathbf{G}_k \mathbf{m}_k + \boldsymbol{\epsilon}_k,$$

which can be solved again with the SVD method. The algorithm for this step is essentially the same as proposed by Bernardino et al. (2002). Note that the data vector \mathbf{d}_k^c contains observed displacements for N interferograms at one pixel, which should not be confused with the definition of \mathbf{d}_i in Eq. (5) which is formed by the displacements of all the pixels of a single interferogram.

Received: 1 May 2019 Accepted: 23 October 2019
Published online: 09 November 2019

References

Acharya HK (1980) Seismic slip on the Philippine fault and its tectonic implications. *Geology* 8(1):40–42

Allen CR (1962) Circum-Pacific faulting in Philippines–Taiwan region. *J Geophys Res* 67(12):4795–4812

Aslan G, Lasserre C, Cakir Z, Ergintav S, Ozarparci S, Dogan U, Bilham R, Renard F (2019) Shallow creep along the 1999 Izmit Earthquake rupture (Turkey) from GPS and high temporal resolution interferometric synthetic aperture radar data (2011–2017). *J Geophys Res* 124(2):2218–2236. <https://doi.org/10.1029/2018jb017022>

Aurelio MA (1992) Tectonique du segment central de la faille Philippine: etude structurale, cinematique et evolution geodynamique. PhD Dissertation. Universite Paris, France

Aurelio MA (2000) Shear partitioning in the Philippines: constraints from Philippine fault and global positioning system data. *Island Arc* 9(4):584–597. <https://doi.org/10.1046/j.1440-1738.2000.00304.x>

Avouac JP (2015) From geodetic imaging of seismic and aseismic fault slip to dynamic modeling of the seismic cycle. *Ann Rev Earth Planet Sci* 43(1):233–271. <https://doi.org/10.1146/annurev-earth-060614-105302>

Bacolcol T (2003) Etude geodesique de la faille Philippine dans les Visayas. PhD Dissertation, Universite Pierre et Marie Curie, France

Bakun WH (1999) Seismic activity of the San Francisco Bay region. *Bull Seismol Soc Am* 89(3):764–784

Bakun WH, Aagaard B, Dost B, Ellsworth WL, Hardebeck JL, Harris RA, Ji C, Johnston MJS, Langbein J, Lienkaemper JJ, Michael AJ, Murray JR, Nadeau RM, Reasenber PA, Reichle MS, Roeloffs EA, Shakal A, Simpson RW, Waldhauser F (2005) Implications for prediction and hazard assessment from the 2004 Parkfield earthquake. *Nature* 437(7061):969–974. <https://doi.org/10.1038/nature04067>

Barbot S, Lapusta N, Avouac JP (2012) Under the hood of the earthquake machine: toward predictive modeling of the seismic cycle. *Science* 336(6082):707–710. <https://doi.org/10.1126/science.1218796>

Barrier E, Huchon P, Aurelio M (1991) Philippine fault—a key for Philippine kinematics. *Geology* 19(1):32–35

Bautista MLP, Oike K (2000) Estimation of the magnitudes and epicenters of Philippine historical earthquakes. *Tectonophysics* 317(1–2):137–169. [https://doi.org/10.1016/S0040-1951\(99\)00272-3](https://doi.org/10.1016/S0040-1951(99)00272-3)

Berardino P, Fornaro G, Lanari R, Sansosti E (2002) A new algorithm for surface deformation monitoring based on small baseline differential SAR interferograms. *IEEE Trans Geosci Rem Sens* 40(11):2375–2383. <https://doi.org/10.1109/Tgrs.2002.803792>

Berkeley Digital Seismic Network (2014) UC Berkeley Seismological Laboratory Dataset. <https://doi.org/10.7932/BDSN>

Besana GM, Ando M (2005) The central Philippine Fault Zone: location of great earthquakes, slow events, and creep activity. *Earth Planets Space* 57(10):987–994. <https://doi.org/10.1186/BF03351877>

Biggs J, Bergman E, Emmerson B, Funning GJ, Jackson J, Parsons B, Wright TJ (2006) Fault identification for buried strike-slip earthquakes using InSAR: the 1994 and 2004 Al Hoceima, Morocco earthquakes. *Geophys J Int* 166(3):1347–1362. <https://doi.org/10.1111/j.1365-246X.2006.03071.x>

Bogiatzis P, Ishii M (2016) DigitSeis: a new digitization software for analog seismograms. *Seismol Res Lett* 87(3):726–736. <https://doi.org/10.1785/0220150246>

- Bolt BA, Miller RD (1975) Catalogue of earthquakes in northern California and adjoining areas; 1 January 1910–31 December 1972
- Bürgmann R, Fielding E, Sukhatme J (1998) Slip along the Hayward fault, California, estimated from space-based synthetic aperture radar interferometry. *Geology* 26(6):559–562
- Çakir Z, Akoglu AM, Belabbes S, Ergintav S, Meghraoui M (2005) Creeping along the ismetpaşa section of the north anatolian fault (western turkey): rate and extent from insar. *Earth Planet Sci Lett* 238(1–2):225–234. <https://doi.org/10.1016/j.epsl.2005.06.044>
- Cakir Z, Ergintav S, Ozener H, Dogan U, Akoglu AM, Meghraoui M, Reilinger R (2012) Onset of aseismic creep on major strike-slip faults. *Geology* 40(12):1115–1118. <https://doi.org/10.1130/G33522.1>
- Catane JP, Kanbara H, Obara K, Sugiwaru N, Hirose K, Olivari RO, Salvador J, Litanas M, Dupio A, Lanuza L (2000) Deformation in the Leyte geothermal production field, Philippines between 1991–1999. In: *Proceeding on World geothermal congress, Japan*, pp 1031–1035
- Chen CW, Zebker HA (2000) Network approaches to two-dimensional phase unwrapping: intractability and two new algorithms. *J Optical Soc Am* 17(3):401–414. <https://doi.org/10.1364/Josaa.17.000401>
- Chen T, Lapusta N (2009) Scaling of small repeating earthquakes explained by interaction of seismic and aseismic slip in a rate and state fault model. *J Geophys Res*. <https://doi.org/10.1029/2008jb005749>
- CRED, Sapir DG (2001) EM-DAT: the emergency events database, Université Catholique de Louvain
- Di Giacomo D, Engdahl E, Storchak D (2018) The ISC-GEM earthquake catalogue (1904–2014): status after the extension project. *Earth Syst Sci Data* 10:1877–1899. <https://doi.org/10.5194/essd-10-1877-2018>
- Donnellan A, Parker J, Hensley S, Pierce M, Wang J, Rundle J (2014) UAVSAR observations of triggered slip on the Imperial, Superstition Hills, and East Elmore Ranch Faults associated with the 2010 M 7.2 El Mayor-Cucapah earthquake. *Geochem Geophys Geosyst* 15(3):815–829. <https://doi.org/10.1002/2013gc005120>
- Doubré C, Peltzer G (2007) Fluid-controlled faulting process in the Asal Rift, Djibouti, from 8 yr of radar interferometry observations. *Geology* 35(1):69–72. <https://doi.org/10.1130/G23022a.1>
- Duquesnoy T, Barrier E, Kasser M, Aurelio M, Gaulon R, Punongbayan RS, Rangin C, Bautista BC, Delacruz E, Isada M, Marc S, Puertollano J, Ramos A, Prevot M, Dupio A, Eto I, Sajona FG, Rigor D, Delfin FG, Layugan D (1994) Detection of creep along the Philippine Fault—1st results of geodetic measurements on Leyte-Island, central Philippine. *Geophys Res Lett* 21(11):975–978. <https://doi.org/10.1029/94gl00640>
- Fattahi H, Amelung F (2016) InSAR observations of strain accumulation and fault creep along the Chaman Fault system, Pakistan and Afghanistan. *Geophys Res Lett* 43(16):8399–8406. <https://doi.org/10.1002/2016gl070121>
- Fujiwara S, Nishimura T, Murakami M, Nakagawa H, Tobita M, Rosen PA (2000) 2.5-D surface deformation of M6.1 earthquake near Mt Iwate detected by SAR interferometry. *Geophys Res Lett* 27(14):2049–2052. <https://doi.org/10.1029/1999GL011291>
- Fukahata Y, Wright TJ (2008) A non-linear geodetic data inversion using ABIC for slip distribution on a fault with an unknown dip angle. *Geophys J Int* 173(2):353–364
- Fukushima Y, Hooper A (2011) Crustal deformation after 2004 Niigataken-chuetsu earthquake, central Japan, investigated by persistent scatterer interferometry. *J Geodetic Soc Japan* 57:195–214
- Galgana G, Hamburger M, McCaffrey R, Corpuz E, Chen QZ (2007) Analysis of crustal deformation in Luzon, Philippines using geodetic observations and earthquake focal mechanisms. *Tectonophysics* 432(1–4):63–87. <https://doi.org/10.1016/j.tecto.2006.12.001>
- Gervasio FC (1967) Age and nature of orogenesis of Philippines. *Tectonophysics* 4(4–6):379–402. [https://doi.org/10.1016/0040-1951\(67\)90006-6](https://doi.org/10.1016/0040-1951(67)90006-6)
- Harris RA (2017) Large earthquakes and creeping faults. *Rev Geophys* 55(1):169–198. <https://doi.org/10.1002/2016rg000539>
- Hsu L, Bürgmann R (2006) Surface creep along the Longitudinal Valley fault, Taiwan from InSAR measurements. *Geophys Res Lett*. <https://doi.org/10.1029/2005gl024624>
- Hussain E, Wright TJ, Walters RJ, Bekaert D, Hooper A, Houseman GA (2016) Geodetic observations of postseismic creep in the decade after the 1999 Izmit earthquake, Turkey: implications for a shallow slip deficit. *J Geophys Res* 121(4):2980–3001. <https://doi.org/10.1002/2015jb012737>
- Jarvis A, Reuter HI, Nelson A, Guevara E (2008) Hole-filled SRTM data V4, available from the CGIAR-CSI SRTM 90m Database. <http://srtm.csi.cgiar.org>
- Jolivet R, Lasserre C, Doin MP, Guillaso S, Peltzer G, Dailu R, Sun J, Shen ZK, Xu X (2012) Shallow creep on the Haiyuan Fault (Gansu, China) revealed by SAR Interferometry. *J Geophys Res Solid Earth*. <https://doi.org/10.1029/2011jb008732>
- Kaduri M, Gratier JP, Renard F, Cakir Z, Lasserre C (2017) The implications of fault zone transformation on aseismic creep: example of the north anatolian fault, turkey. *J Geophys Res* 122(6):4208–4236. <https://doi.org/10.1002/2016jb013803>
- Kaneko Y, Fialko Y, Sandwell DT, Tong X, Furuya M (2013) Interseismic deformation and creep along the central section of the North Anatolian Fault (Turkey): inSAR observations and implications for rate-and-state friction properties. *J Geophys Res* 118(1):316–331. <https://doi.org/10.1029/2012jb009661>
- Lindsey EO, Fialko Y, Bock Y, Sandwell DT, Bilham R (2014a) Localized and distributed creep along the southern San Andreas Fault. *J Geophys Res* 119:7909–7922. <https://doi.org/10.1002/2014JB011275>
- Lindsey EO, Sahakian VJ, Fialko Y, Bock Y, Barbot S, Rockwell KT (2014b) Interseismic strain localization in the San Jacinto Fault Zone. *Pure Appl Geophys* 171(11):2937–2954. <https://doi.org/10.1007/s00024-013-0753-z>
- Louie JN, Allen CR, Johnson DC, Haase PC, Cohn SN (1985) Fault slip in Southern-California. *Bull Seismol Soc Am* 75(3):811–833
- Lumbang R, Hurukawa N (2014) Relocation of large earthquakes along the Philippine Fault Zone and their fault planes. *Bull Int Instit Seismol Earthq Eng* 48:43–48
- McComb HE, Wenner F (1936) Shaking-table investigations of teleseismic seismometers. *Bull Seismol Soc Am* 26(4):291–316
- Mitsui Y (2018) Elastic interaction of parallel rate-and-state-dependent frictional faults with aging and slip laws: slow-slip faults can sometimes host fast events. *Earth Planets Space*. <https://doi.org/10.1186/s40623-018-0911-8>
- Murayama Y, Si Hirano (1993) The damage and the rehabilitation process after 1990 Luzon Earthquake—some cases of la Union and Nueva Ecija—. The science reports of the Tohoku University 7th series. *Geography* 43(1):27–48
- Nadeau RM, Johnson LR (1998) Seismological studies at parkfield vi: moment release rates and estimates of source parameters for small repeating earthquakes. *Bull Seismol Soc Am* 88(3):790–814
- Nakata T, Tsutsumi H, Punongbayan RS, Rimando RE, Daligdig J, Daag A (1990) Surface faulting associated with the Philippine earthquake of 1990. *J Geogr* 99:95–112 (in Japanese with English abstract)
- National Research Institute for Earth Science and Disaster Resilience (2019) NIED F-net. National Research Institute for Earth Science and Disaster Resilience. <https://doi.org/10.17598/NIED.0005>
- Natsuaki R, Nagai H, Motohka T, Ohki M, Watanabe M, Thapa RB, Tadono T, Shimada M, Suzuki S (2016) SAR interferometry using ALOS-2 PALSAR-2 data for the Mw 7.8 Gorkha, Nepal earthquake. *Earth Planets Space* 68:1–13. <https://doi.org/10.1186/s40623-016-0394-4>
- Noda H, Lapusta N (2013) Stable creeping fault segments can become destructive as a result of dynamic weakening. *Nature* 493(7433):518–521. <https://doi.org/10.1038/nature11703>
- Peng ZG, Gombert J (2010) An integrated perspective of the continuum between earthquakes and slow-slip phenomena. *Nat Geosci* 3(9):599–607. <https://doi.org/10.1038/Ngeo940>
- PHIVOLCS (2003) Masbate earthquake QRT investigation. Philippine Institute of Volcanology and Seismology Annual Report 2003
- PHIVOLCS (2018) Philippine Institute of Volcanology and Seismology—Department of Science and Technology (PHIVOLCS-DOST). *Earthquake Catalogue of the Philippines from 1600–2017*
- Pousse Beltran L, Pathier E, Jouanne F, Vassallo R, Reinoza C, Audemard F, Doin MP, Volat M (2016) Spatial and temporal variations in creep rate along the El Pilar fault at the Caribbean-South American plate boundary (Venezuela), from InSAR. *J Geophys Res* 121(11):8276–8296. <https://doi.org/10.1002/2016jb013121>
- Priou R, Cornet FH, Dorbath C, Dorbath L, Ogena M, Ramos E (2000) An induced seismicity experiment across a creeping segment of the Philippine Fault. *J Geophys Res* 105(B6):13,595–13,612. <https://doi.org/10.1029/2000jb900052>
- Rangin C, Le Pichon X, Mazzotti S, Pubellier M, Chamotrooke N, Aurelio M, Walpersdorf A, Quebral R (1999) Plate convergence measured by GPS across the Sundaland/Philippine sea plate deformed boundary: the

- Philippines and eastern Indonesia. *Geophys J Int* 139(2):296–316. <https://doi.org/10.1046/j.1365-246x.1999.00969.x>
- Romanet P, Bhat HS, Jolivet R, Madariaga R (2018) Fast and slow slip events emerge due to fault geometrical complexity. *Geophys Res Lett* 45(10):4809–4819. <https://doi.org/10.1029/2018GL077579>
- Ryder I, Bürgmann R (2008) Spatial variations in slip deficit on the central San Andreas Fault from InSAR. *Geophys J Int* 175(3):837–852. <https://doi.org/10.1111/j.1365-246X.2008.03938.x>
- SEASSEE (1985) Series on Seismology, Vol. IV: Philippines. Government Printing Office, Washington D. C
- Shaw BE, Dieterich JH (2007) Probabilities for jumping fault segment stepovers. *Geophys Res Lett*. <https://doi.org/10.1029/2006gl027980>
- Shibutani T (1991) Search for the buried subfault(s) of the 16 July 1990 Luzon Earthquake, the Philippines using aftershock observations. *J Nat Disaster Sci* 13(1):29–38
- Shirzaei M, Bürgmann R (2013) Time-dependent model of creep on the Hayward fault from joint inversion of 18 years of InSAR and surface creep data. *J Geophys Res* 118(4):1733–1746. <https://doi.org/10.1002/jgrb.50149>
- Silcock DM, Beavan J (2001) Geodetic constrains on coseismic rupture during the 1990 M_s 7.8 Luzon, Philippines, earthquake. *Geochem Geophys Geosyst* 2:101
- Takada Y, Sagiya T, Nishimura T (2018) Interseismic crustal deformation in and around the Atotsugawa fault system, central Japan, detected by InSAR and GNSS. *Earth Planets Space* 70:32. <https://doi.org/10.1186/s40623-018-0801-0>
- Thomas MY, Avouac JP, Champenois J, Lee JC, Kuo LC (2014a) Spatiotemporal evolution of seismic and aseismic slip on the Longitudinal Valley Fault, Taiwan. *J Geophys Res* 119(6):5114–5139. <https://doi.org/10.1002/2013jb010603>
- Thomas MY, Avouac JP, Gratier JP, Lee JC (2014b) Lithological control on the deformation mechanism and the mode of fault slip on the Longitudinal Valley Fault, Taiwan. *Tectonophysics* 632:48–63. <https://doi.org/10.1016/j.tecto.2014.05.038>
- Tsutsumi H, Perez JS (2013) Large-scale active fault map of the Philippine fault based on aerial photograph interpretation. *Active Fault Res* 39:29–37. https://doi.org/10.11462/afr.2013.39_29
- Tsutsumi H, Perez JS, Marjes JU, Papiona KL, Ramos NT (2015) Coseismic displacement and recurrence interval of the 1973 Ragay Gulf earthquake, southern Luzon, Philippines. *J Disaster Res* 10(1):83–90
- Tsutsumi H, Perez JS, Lienkaemper JJ (2016) Variation of surface creep rate along the Philippine fault based on surveys of alignment arrays and offset cultural features. Fall Meeting of American Geophysical Union, San Francisco
- Uchida N, Bürgmann R (2019) Repeating earthquakes. *Ann Rev Earth Planet Sci*. <https://doi.org/10.1146/annurev-earth-053018-060119>
- Uchida N, Matsuzawa T, Ellsworth WL, Imanishi K, Shimamura K, Hasegawa A (2012) Source parameters of microearthquakes on an interplate asperity off Kamaishi, NE Japan over two earthquake cycles. *Geophys J Int* 189(2):999–1014. <https://doi.org/10.1111/j.1365-246X.2012.05377.x>
- Wegmüller U, Werner C (1997) Gamma SAR processor and interferometry software. In: Proceedings of 3rd ERS symposium, space service environment (Spec. Publ. 414), vol 3, pp 1687–1692
- Wells DL, Coppersmith KJ (1994) New empirical relationships among magnitude, rupture length, rupture width, rupture area, and surface displacement. *Bull Seismol Soc Am* 84(4):974–1002
- Yamazaki J (2001) Seismic observation by the Wiechert seismograph at Abuyama Observatory. *Zisin (Journal of the Seismological Society of Japan 2nd ser)* 53(3):303–312
- Yang YH, Tsai MC, Hu JC, Aurelio MA, Hashimoto M, Escudero JAP, Su Z, Chen Q (2018) Coseismic slip deficit of the 2017 Mw 6.5 Ormoc Earthquake that occurred along a creeping segment and geothermal field of the Philippine Fault. *Geophys Res Lett* 45(6):2659–2668. <https://doi.org/10.1002/2017gl076417>

Publisher's Note

Springer Nature remains neutral with regard to jurisdictional claims in published maps and institutional affiliations.

Submit your manuscript to a SpringerOpen® journal and benefit from:

- Convenient online submission
- Rigorous peer review
- Open access: articles freely available online
- High visibility within the field
- Retaining the copyright to your article

Submit your next manuscript at ► [springeropen.com](https://www.springeropen.com)
